ELSEVIER

Contents lists available at ScienceDirect

# Remote Sensing of Environment

journal homepage: www.elsevier.com/locate/rse



Adaptive optical algorithms with differentiation of water bodies based on varying composition of suspended particulate matter: A case study for estimating the particulate organic carbon concentration in the western Arctic seas



Dariusz Stramski <sup>a,\*</sup>, Sorin Constantin <sup>b,c</sup>, Rick A. Reynolds <sup>a</sup>

- <sup>a</sup> Marine Physical Laboratory, Scripps Institution of Oceanography, University of California San Diego, La Jolla, CA 92093-0238, USA
- <sup>b</sup> Research Institute of the University of Bucharest, 050663 Bucharest, Romania
- <sup>c</sup> Terrasigna, 020581 Bucharest, Romania

#### ARTICLE INFO

Edited by Menghua Wang

Keywords:
Ocean optical properties
Inherent optical properties
Remote-sensing reflectance
Marine suspended particles
Particulate organic carbon

Particulate composition

#### ABSTRACT

High complexity and variability in composition of water constituents pose major challenges for development of algorithms to estimate biogeochemical data products from optical observations over the continuum of diverse aquatic environments. To address these challenges, we examined an adaptive optical approach that accounts for variability in composition of suspended particulate matter. We use the ratio of particulate organic carbon to suspended particulate matter concentration, POC/SPM, for optically discriminating water bodies with varying proportions of organic and mineral particles. Through the analysis of field data from the western Arctic seas that exhibit a broad range of water composition and optical properties, we developed empirical algorithms to estimate SPM and POC/SPM either from the particulate inherent optical properties (IOPs) of seawater, i.e., the spectral particulate absorption  $a_p(\lambda)$  or backscattering  $b_{bp}(\lambda)$  coefficients, or directly from the spectral remotesensing reflectance of the ocean,  $R_{IS}(\lambda)$ . The capability to retrieve POC/SPM from optical measurements was used to formulate the particle composition-specific algorithms for estimating POC from particulate IOPs or  $R_{18}(\lambda)$ . The evaluation of algorithms with the development field dataset demonstrates that the algorithm formulations accounting for changes in POC/SPM provide significant improvements in POC estimates along the continuum of optically-complex Arctic waters compared with algorithms that do not account for variations in particulate composition, such as the current standard POC algorithm used for global satellite applications. The results of example application of the particle composition-specific algorithm and standard global algorithm to satellite observations are consistent with comparisons of these algorithms for our field dataset, which supports a conclusion that the standard algorithm tends to overestimate POC in Arctic waters that exhibit a broad range of particle composition. Although this study demonstrates the adaptive approach using data from the Arctic region, it has broader significance and is amenable to further enhancements by including other optically-derivable water constituent properties. Further validation analyses and efforts are needed towards a unified approach with improved representation of cause-and-effect relationships between water composition and optical properties to enable improved optically-based applications across a wide range of water bodies.

## 1. Introduction

Improvements in the estimation of biogeochemically important constituents and properties of aquatic environments from inherent or apparent optical properties of water bodies is one of the main prerequisites to further advance the applications of optical measurements in

aquatic sciences, including the use of in situ optical measurements as well as satellite and airborne remote sensing observations of the world's oceans. This challenge arises largely from a complex composition of optically-significant constituents of seawater and intricate linkages between the optical properties of various in-water constituents and a combination of many physical, biological, chemical, and geological

E-mail address: dstramski@ucsd.edu (D. Stramski).

<sup>\*</sup> Corresponding author.

processes that control the sources, variability, and fates of the constituents. Currently, new satellite ocean color missions with significantly enhanced capabilities of optical measurements are in the phase of preparation for launch, such as NASA's Plankton, Aerosol, Cloud, ocean Ecosystem (PACE) mission with high-spectral resolution and polarization capabilities to be launched in 2024 (Werdell et al., 2019). The missions such as PACE are expected to result in significant improvements of satellite retrievals of spectral remote-sensing reflectance of the ocean,  $R_{rs}(\lambda)$ , and spectral inherent optical properties (IOPs) of seawater constituents (where  $\lambda$  is light wavelength in vacuum). To unlock the full potential of these advancements in support of remote sensing science and applications, novel algorithmic approaches are needed with improved representation of interactions between light and the highly complex and variable constituent composition of seawater. One research area where interactions of light with a complex mix of water constituents can be described at a higher level of mechanistic detail than in extant bio-optical or remote-sensing algorithms is associated with the composition of suspended particulate matter, especially the proportions of organic and inorganic particles within particulate assemblages.

Because of high level of optical complexity and diversity caused by variability in concentrations and composition of water constituents, it is unlikely that a single bio-optical or remote-sensing algorithm, regardless of its underlying empirical, semi-analytical or analytical approach, can perform adequately over the continuum of various aquatic environments. The global algorithms for estimating the concentrations of chlorophyll-a (Chla) and particulate organic carbon (POC) from satellite ocean color observations (O'Reilly et al., 1998; O'Reilly and Werdell, 2019; Stramski et al., 2008; Stramski et al., 2022) were formulated under the premise of acceptable performance in waters with optical properties driven primarily by phytoplankton and covarying organic materials (Gordon and Morel, 1983; Morel and Prieur, 1977). These global algorithms are applied to diverse water bodies indiscriminately with respect to composition of seawater constituents, which can yield large errors in Chla or POC products in various environmental scenarios, for example high proportion of mineral particles in suspended particulate matter (Woźniak and Stramski, 2004). Numerous approaches have been proposed to address the challenges of optical remote sensing across diverse environments that exhibit the complexities of water composition and optical properties (e.g., Matthews, 2011; Odermatt et al., 2012; Tyler et al., 2016). Many studies have focused on regionally-specific algorithms whose parameterizations, usually empirical, have been optimized using regional datasets. Some of these algorithms include the use of predefined limits to the applicability or a switching scheme with predefined threshold values applied to the reflectance or water constituent concentrations to broaden the range of applicability across diverse conditions. Over the last 2 decades the adaptive approaches based on an optical water type (OWT) classification have emerged as a prospective framework under which to conduct interpretive analysis and develop generalized algorithms for applications along the continuum of diverse optical and biogeochemical conditions encompassing open ocean, coastal, and inland aquatic environments (e.g., Eleveld et al., 2017; Lahet et al., 2001; Le et al., 2011; Lubac and Loisel, 2007; Mélin et al., 2011; Mélin and Vantrepotte, 2015; Moore et al., 2001, 2009, 2014; Neil et al., 2019; Reinart et al., 2003; Spyrakos et al., 2018; Vantrepotte et al., 2012; Ye et al., 2016). The OWT classification schemes in aquatic remote sensing are commonly based on in situ and/ or satellite reflectance data which serve to differentiate water types in terms of key features associated with the spectral shape and/or magnitude of reflectance. A number of studies support the emerging view that such optical classification framework for blending the retrievals from multiple class-specific algorithms has significant potential to improve the overall accuracy of remote-sensing data products across a wide range of water bodies and to make progress towards a unified approach for global applications (e.g., Le et al., 2011; Moore et al., 2014; Neil et al., 2019; Vantrepotte et al., 2012; Xue et al., 2019).

The variations in ocean color, or more generally the aquatic color,

captured by remote-sensing reflectance measurements depend on water IOPs which, in turn, are driven in a complex fashion by concentration and composition of various particulate and dissolved water constituents that are highly variable in time and space. In the reflectance-based classification schemes the optical effects of various types of coexisting water constituents are not explicitly separable or quantifiable. One consequential result is that a given reflectance-based class can encompass large variation in composition of water constituents that have different optical properties, such as large variation in proportions of organic and mineral suspended particles (Spyrakos et al., 2018; Vantrepotte et al., 2012). Under such circumstances, the reflectance classspecific algorithms aimed, for example, at retrieving data products associated solely with organic particulate matter such as POC or Chla, can be inadequate within or across environments where the organic vs. mineral composition of particulate matter varies substantially. Therefore, there is a need to explore alternative approaches that can differentiate the aquatic environments at a more fundamental level describing the composition of optically significant water constituents, in particular the composition of suspended particulate matter (Neukermans et al.,

The optical effects of particles suspended in water depend, to first order, on the concentration, composition, and size distribution of particles (e.g., Jerlov, 1976; Jonasz and Fournier, 2007; Morel, 1973). In this study we investigate an optically-based approach that addresses variations in optical effects produced by changes in the composition of particulate matter, specifically the relative contributions of organic and mineral particles coexisting in water. These two main categories of particles have generally quite different refractive index, especially plankton cells and mineral particles (Aas, 1996). Such differences in refractive index have major implications to interactions of light with particles and, hence, to the bulk optical properties of marine particle assemblages (e.g., Babin et al., 2003a; Bowers and Binding, 2006; Morel, 1973; Twardowski et al., 2001; Stramski and Kiefer, 1991). It has long been recognized that the ratio POC/SPM, where SPM is the total mass concentration of suspended particulate matter, can serve as a proxy of particulate composition which aids in the interpretation of variability in light scattering properties of seawater (Betzer et al., 1974; Carder et al., 1974; Feely et al., 1974). Although POC represents a fraction of particulate organic matter (POM) and there is no single conversion factor from POC to POM due to some variations in the composition of POM, the POC/SPM ratio is a useful proxy for characterizing the contribution of organic particles to SPM. The carbon content of POM is the structural foundation of particulate organic matter and the variability in POC/POM is generally constrained within a relatively narrow range between about 0.4 and 0.55 (Babin et al., 2003a; Feely et al., 1974; Gordon, 1970; Riley, 1970). In addition, carbon is a major "currency" in the study of the Earth's biogeochemical cycles, so direct use of POC has advantages over POM for research that aims to advance the estimation of carbon data products from optical algorithms.

In the present study we use POC/SPM as a proxy of particulate composition but, in general, the question whether POC/SPM or POM/ SPM (or alternatively PIM/SPM where PIM is the mass concentration of inorganic particulate matter) is chosen as composition-related parameter for optical studies can depend on specific or long-term research goals. Previous studies of different water bodies demonstrated that the overall variability in particulate IOPs is reduced and the relationships between the IOPs and particle concentration or particle size metrics are improved if the analysis is constrained by the compositional parameters such as POC/SPM or POM/SPM (Loisel et al., 2007; Neukermans et al., 2012; Reynolds et al., 2016; Snyder et al., 2008; Stavn and Richter, 2008; Stramski et al., 2007; Woźniak et al., 2010; Woźniak et al., 2018; Woźniak and Meler, 2020). It is also notable that the benefit of POC/ SPM as a relatively simple metric can extend beyond the effects associated with varying organic vs. mineral composition. Our previous analysis of measurements in the western Arctic seas indicated a significant degree of covariation between POC/SPM and the contributions of differently-sized particles to particle size distribution (PSD) (Reynolds et al., 2016). Specifically, the organic-dominated particle assemblages (high POC/SPM) exhibited consistently higher proportion of large-sized particles (for example,  $>20~\mu m$  in size) compared to mineral-dominated assemblages (low POC/SPM). Such covariation has the potential to strengthen the usefulness of POC/SPM metric because PSD is also an important particle characteristic affecting the optical properties.

The present study has three main objectives: (i) to investigate the POC/SPM ratio as a proxy of composition of suspended particulate matter for optically discriminating water bodies dominated by organic particles, mineral particles, or mixed particle assemblages; (ii) to formulate algorithms for estimating SPM and the POC/SPM ratio from optical measurements of particulate IOPs or remote-sensing reflectance  $R_{rs}(\lambda)$ , and (iii) to formulate adaptive particle composition-specific algorithms for estimating POC based on optical measurements of particulate IOPs or  $R_{rs}(\lambda)$ , which account for variations in POC/SPM. These objectives are addressed through the analysis of field data collected in the western Arctic seas exhibiting a broad range of variability in particulate characteristics and optical properties of seawater. Using this algorithm development dataset, we also evaluated how well the different algorithms represent the variability within this dataset. The validation and performance assessment of the algorithms with independent field and satellite data is a separate extensive topic which is beyond the scope of this study and is expected to be addressed in future

## 2. Methods

## 2.1. Study area and data sources

This study is based on measurements made during four oceanographic cruises in the Arctic region encompassing the Chukchi Sea and the western Beaufort Sea (Fig. 1). The first cruise was in summer 2009 (31 July – 24 August) in the southeastern Beaufort Sea which included the region of Mackenzie River plume. This was the MALINA (MAckenzie LIght aNd cArbon) expedition on the *CCGS Amundsen* (Massicotte et al., 2021). The next two cruises (HLY1001 and HLY1101) were on the

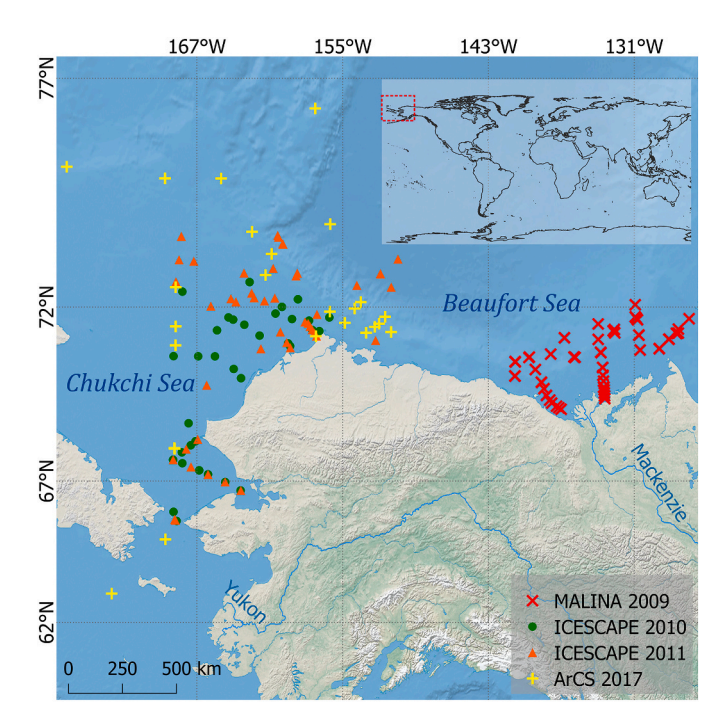


**Fig. 1.** Locations of oceanographic stations where coincident measurements of optical properties and characteristics of suspended particulate matter were collected. The data were collected during four cruises as indicated.

*USCGC Healy* and took place in summer seasons of 2010 (18 June -16 July) and 2011 (28 June - 24 July) in the Chukchi Sea and western Beaufort Sea. These two cruises were part of the NASA ICESCAPE (Impacts of Climate on EcoSystems and Chemistry of the Arctic Pacific Environment) program (Arrigo, 2015) and are referred to as ICESCAPE cruises. The fourth cruise (MR17-05C) was in late summer 2017 (23 August - 21 September) and also surveyed the region of the Chukchi and Beaufort Seas. This cruise was on the R/V Mirai as part of the Japanese Arctic Challenge for Sustainability (ArCS) program (Shiozaki et al., 2019). This cruise is referred to as ArCS.

In this study we use a dataset assembled from both in situ measurements and analysis of discrete water samples that were collected in close proximity to location and time of in situ measurements. The data were collected over a broad range of environments using a consistent set of measurement and data processing protocols. The data quality assurance and control processes were integrated into the development of the final dataset. Portions of this dataset have been described in our previous studies which address relationships between seawater optical properties and various concentration-, size-, and composition-related characteristics of suspended particulate matter (Neukermans et al., 2016; Reynolds et al., 2016; Reynolds and Stramski, 2019; Runyan et al., 2020).

Data collected from a total of 139 stations sampled during the four Arctic cruises are utilized in this study (Fig. 1). The key optical variables involved in our analysis include two IOPs, namely the spectral particulate absorption coefficient,  $a_p(\lambda)$ , and the spectral particulate backscattering coefficient,  $b_{\rm bp}(\lambda)$ , as well as  $R_{\rm rs}(\lambda)$  which belongs to the category of apparent optical properties (AOPs) and is central to remote sensing (Mobley, 1994; Preisendorfer, 1961). The key particulate characteristics analyzed in this study are POC and SPM; however, for general characterization of investigated water bodies we also report on Chla data. For the analysis of relationships between the particulate characteristics and IOPs, data were collected at near surface depths ( $\sim$ 1–5 m) and a few additional depths. These additional sampling depths were selected to obtain data for water samples where the maximum of chlorophyll-a fluorescence, the optical beam attenuation coefficient, or backscattering coefficient occurred within the water column, and also close to the bottom (within 3-5 m) at stations located on the shelf.

The final basic dataset in this study consists of 335 matchup measurements of POC, SPM, and  $a_p(\lambda)$ . Out of these 335 measurements, about 50% represent near-surface samples, specifically 158 between the sea surface and 5 m depth and additional 8 samples between 5 and 10 m. Out of the remaining 169 samples, 121 samples were collected between 10 and 50 m, 27 between 50 and 100 m, and 21 between 100 and 300 m. The deepest depths were sampled at stations located off the shelf. Within this basic dataset the number of matchup measurements which additionally include  $b_{bp}(\lambda)$  is smaller, for example 294 matchups for  $b_{\rm bp}(550)$ ,  $a_{\rm p}(\lambda)$ , POC, and SPM. The dataset that includes measurements at near-surface depths and larger depths is used in this study for the analysis of relationships between particulate IOPs and particulate concentration and composition characteristics. For the analysis of relationships between  $R_{rs}(\lambda)$  and particulate characteristics, only the nearsurface measurements are used. In this case the number of matchup measurements is 98.

# 2.2. Bulk measures of particle mass concentration and composition

Immediately upon collection of water samples at discrete depths from a CTD-Rosette equipped with Niskin bottles, the samples were prepared and stored on board the ship for post-cruise analysis of the mass concentrations of dried suspended particulate matter (SPM in units of mg m<sup>-3</sup>), particulate organic carbon (POC in mg m<sup>-3</sup>), and chlorophyll-a (Chla in mg m<sup>-3</sup>). A detailed description of the methodology of water sample collection and analysis for MALINA and ICE-SCAPE cruises is provided in Reynolds et al. (2016) and Reynolds and Stramski (2019). The methodology on the ArCS cruise was essentially

the same. In summary, filtration volumes to prepare the SPM, POC, and Chla samples ranged from tens of milliliters to over 10 L. This range reflects the adjustment of filtration volume dependent on particle concentration in water in order to optimize each individual analysis. The SPM samples were prepared by collection of particles onto pre-rinsed, pre-combusted, and pre-weighed glass-fiber GF/F filters (25 mm diameter). The SPM values were determined post-cruise using a standard gravimetric method (Van der Linde, 1998) by measuring the dry mass of particles with a Mettler-Toledo MT5 microbalance with 1 µg precision. POC determinations were made using a method consistent with JGOFS protocols (Intergovernmental Oceanographic Commission, 1994). Samples were prepared by collecting particles on pre-combusted 25 mm GF/F filters, followed by drying and storing the sample filters for postcruise analysis. The filtered volumes and the associated load of POCcontaining particles on filters were appropriately large to minimize the contribution of adsorbed dissolved organic carbon compared to POC (Novak et al., 2018). POC was determined with standard CHN analysis that involves high temperature combustion of sample filters (Parsons et al., 1984). The filters were subject to acidification treatment prior to CHN analysis. Similar analysis was made to determine the background organic carbon content on unused (blank) pre-combusted filters from the same lot of filters that were used to prepare samples. The carbon measurements on sample filters were corrected for the average amount of background carbon determined from several blank filters. The potential sources of uncertainties in POC determinations are discussed in Gardner et al. (2003) and IOCCG Protocol Series (2021).

The final data of SPM and POC were usually obtained by averaging results of duplicate or triplicate samples. The median coefficient of variation for replicate samples of SPM varied between about 3% and 6% for samples collected on different cruises. A similar range of 2% to 5% was measured for replicate samples of POC. During the process of data quality control, we excluded samples with POC < 20 mg m $^{-3}$  measured during the MALINA campaign because the reproducibility between the replicates for these very low POC samples was significantly reduced. In addition, our final dataset excludes six measurements with POC/SPM ratio higher than 0.6. Such values of POC/SPM are likely biased high owing to measurement uncertainties in POC and/or SPM. The POC/SPM ratio is dimensionless and was determined on a g:g (gram by gram) basis.

Samples were also collected on 25 mm GF/F filters for phytoplankton pigment analysis. This analysis was made with High Performance Liquid Chromatography (HPLC) as described in Ras et al. (2008) or Van Heukelem and Thomas (2001). In this study we report on the concentration of total chlorophyll-a (Chla) which is a sum of mono- and divinyl chlorophyll-a, chlorophyllide-a, and the allomeric and epimeric forms of chlorophyll-a.

# 2.3. Optical measurements of particulate IOPs and remote-sensing reflectance

The spectral absorption coefficient of particles,  $a_p(\lambda)$  (in units of m<sup>-1</sup>), was measured on discrete water samples obtained from the CTD-Rosette deployments. Measurements of spectral backscattering coefficient of particles,  $b_{bp}(\lambda)$  (in units of m<sup>-1</sup>), were collected in situ through vertical profiling with a submersible instrument package. The methodology of these IOP measurements is described in Reynolds et al. (2016) and Reynolds and Stramski (2019). Here we provide a brief summary.

The determinations of  $a_p(\lambda)$  were made with a spectrophotometric filter-pad method using a measurement configuration with samples inside the integrating sphere which ensures the highest accuracy of measurements with the filter-pad method (Stramski et al., 2015; Roesler et al., 2018). The measurements with this method were shown to agree with the PSICAM (Point-Source Integrating Cavity Absorption Meter) method that takes measurements on particle suspensions to within 7% or less in terms of the spectral values of the mean percentage difference (Kostakis et al., 2021). A dual-beam spectrophotometer (Lambda 18,

Perkin Elmer) equipped with a 15 cm integrating sphere (Labsphere) was used. Samples and blank filters were scanned at 1 nm intervals over the spectral range 300–800 nm (MALINA) or 300–850 nm (ICESCAPE, ArCS). The  $a_{\rm p}(\lambda)$  coefficient was calculated following the protocol described in Roesler et al. (2018) including a correction for the pathlength amplification for inside-sphere configuration of filter-pad method determined by Stramski et al. (2015).

In situ measurements of backscattering coefficient were made immediately before or after deployment of CTD-Rosette for collection of water samples. For MALINA, a multispectral Hydroscat-6 sensor was paired with two single-wavelength a-\u00e3eta sensors (HOBI Labs, Inc.) to yield measurements in 8 spectral bands between 420 and 671 nm. On the ICESCAPE and ArCS cruises, the backscattering measurements were made in 11 spectral bands between 394 and 852 nm with two Hydroscat-6 instruments. For intercomparison and data quality assurance both instruments were equipped with a common band centered at 550 nm. The processing of backscattering data and the calculation of both the spectral backscattering coefficient  $b_b(\lambda)$  and the particulate backscattering coefficient,  $b_{\rm bp}(\lambda) = b_{\rm b}(\lambda) - b_{\rm bw}(\lambda)$  where  $b_{\rm bw}(\lambda)$  denotes the contribution of pure seawater, are described in Reynolds et al. (2016). For matching with data obtained from discrete water samples, vertical profile measurements of backscattering were averaged into 0.5 or 1 m depth bins. Previous analysis of backscattering measurements suggests that uncertainties are generally from a few percent to about 10 - 15% and are consistent with the level of agreement observed through comparisons of different instruments (including Hydroscat-6) which use different optical configurations, calibration methods, and data processing methods (Boss et al., 2004; Twardowski et al., 2007). In clear waters where pure seawater makes large contribution to backscattering, the  $b_{\rm bp}(\lambda)$  determinations can be subject to higher uncertainty (Twardowski et al., 2007; Stramski et al., 2008).

The spectral remote-sensing reflectance,  $R_{rs}(\lambda)$ , was determined from in situ radiometric measurements taken shortly after or before deployments of CTD-Rosette and backscattering sensors.  $R_{rs}(\lambda)$  (sr<sup>-1</sup>) is defined as the ratio of the upwelling (i.e., photons traveling along the vertical towards zenith) water-leaving radiance,  $L_{\rm w}(\lambda, z=0^+)$ , to the surface downward plane irradiance,  $E_d(\lambda, z = 0^+) \equiv E_s(\lambda)$ , where these quantities are just above the sea surface, i.e.,  $z = 0^+$  (Mobley, 1994). On the MALINA and ICESCAPE cruises,  $L_w(\lambda, z = 0^+)$  and  $E_s(\lambda)$  were determined from underwater measurements obtained with in situ spectral radiometers and extrapolated to values above the sea surface. A free-falling Compact-Optical Profiling System (Biospherical Instruments, Inc.) was used on the MALINA cruise (Antoine et al., 2013) and Profiling Reflectance Radiometer (PRR-800, Biospherical Instruments, Inc.) was used on the ICESCAPE cruises (Lewis et al., 2016). Both instruments provided data of underwater vertical profiles of upwelling radiance  $L_{\rm u}(\lambda, z)$  and downward plane irradiance  $E_{\rm d}(\lambda, z)$  in 18 spectral bands spanning the ultraviolet (UV), visible (VIS) and nearinfrared (NIR) spectral regions. On the ArCS cruise, a Hyperspectral Optical Profiler (HyperPro, Satlantic, Inc., now SeaBird Scientific) was deployed in a surface float configuration, providing high-spectral resolution measurements between 350 and 800 nm at ~3.3 nm intervals for near-surface  $L_{\rm u}(\lambda,z=0.2~{\rm m})$  and above-surface  $E_{\rm s}(\lambda)$ . The measurements of  $L_{\rm u}(\lambda,z=0.2~{\rm m})$  were extrapolated to above sea surface to obtain  $L_{\rm w}(\lambda,z=0.2~{\rm m})$  $z=0^+$ ). The radiometric measurements, data processing, and subsequent determination of  $R_{rs}(\lambda)$  were generally consistent with recommended protocols (Mueller, 2003; IOCCG Protocol Series, 2019). Methodological details for obtaining the  $R_{rs}(\lambda)$  data used in this study are also described in Zheng et al. (2014) and Uitz et al. (2015). One notable detail of data processing for the ArCS cruise is that the extrapolation of  $L_{II}(\lambda, z = 0.2 \text{ m})$  was supported by depth-resolved measurements taken with an independent Profiling Reflectance Radiometer PRR-800 (Biospherical Instruments, Inc.). The uncertainty of  $R_{rs}(\lambda)$  determinations using the methodology involving the underwater measurements of upwelling radiance are generally expected to be of the order of 5% or less (IOCCG Protocol Series, 2019) although it is notable that the determinations in the long-wavelength portion of the spectrum in clear waters are susceptible to higher uncertainties (Li et al., 2016).

## 2.4. Statistical formulation and evaluation of algorithms

For the purpose of formulating the empirical algorithms to estimate particulate characteristics from optical measurements, the model-I regression analysis is appropriate and was used in the study (Legendre and Michaud, 1999; Ricker, 1973; Sokal and Rohlf, 1995). The numerical parametrizations of algorithm equations obtained from the regression analysis are valid for SPM and POC expressed in units of mg  $\rm m^{-3}$ , the inherent optical coefficients in units of  $\rm m^{-1}$ , and remote-sensing reflectance in  $\rm sr^{-1}$ .

The goodness-of-fit of regression models was evaluated using several statistical parameters characterizing the degree of agreement between the algorithm-derived and measured values from the algorithm development datasets (Table 1). The validation of algorithms with independent field datasets and satellite-in situ matchup datasets is beyond the scope of this study. Such validation analyses are desirable and expected to be conducted in future studies.

Typically, when examining a relationship between the particulate and optical variables underlying any specific algorithm considered in this study, we tested several candidate algorithm formulas involving different light wavelengths. The regression model that best described the measured data was selected based on a comparative analysis of various statistical indicators. The algorithms that provide the best fit to measured data have MdR close to 1 and low values (the closer to zero the better) of MdB, MdAPD, MdSA, and RMSD. We note that similar to MdAPD, the median symmetric accuracy MdSA can be interpreted as a median percentage error but, unlike MdAPD, it does not penalize overand underprediction differently (Morley, 2016; Morley et al., 2018, note that in these articles the median symmetric accuracy is denoted by  $\zeta$ ). In addition, the Pearson correlation coefficient, R, and the linear regression between the algorithm-derived and measured data were determined. In this case a model-II linear regression analysis based on the reduced major axis method was applied (Bellacicco et al., 2019; Kermack and Haldane, 1950; Ricker, 1973). For the variables of POC and SPM the model-II regression analysis and calculations of R were made on log<sub>10</sub>transformed data. In the analysis of algorithm-derived vs. measured values of POC/SPM, the ordinary (untransformed) data were used.

A pair-wise comparison analysis of candidate regression models (Seegers et al., 2018) was also conducted to support the selection of final regression model representing a given relationship. For each pair of compared algorithms, this analysis involved the calculation of differences between the algorithm-derived and measured values for each observation. The algorithm with most wins (i.e., higher number of smallest differences) was considered superior. While the calculations of

**Table 1**Statistical metrics used in characterization of the goodness-of-fit of algorithmic formulas.

Symbol	Description
N	Number of samples (data)
$y_{i,}x_{i}$	Algorithm-derived value $y$ and measured value $x$ for sample $i$ of $N$
S and $I$	Slope and intercept obtained from model-II linear regression of $log(y_i)$ on
	$log(x_i)$ or from model-II linear regression of $y_i$ on $x_i$ . $S=1$ and $I=$
	0 correspond to perfect agreement.
R	Pearson's product moment correlation coefficient between algorithm-
	derived and measured variables or between log-transformed variables
	used in model-II linear regression
MdB	Median bias; median value of $(y_i - x_i)$
MdR	Median ratio of $(y_i / x_i)$
MdAPD	Median absolute percentage difference, median value of $100 \times [ (y_i - x_i)/x_i ]$
MdSA	Median symmetric accuracy in percent, $100 \times [10^{\text{median}[ \log(yi/xi) ]} - 1]$
RMSD	Root mean square deviation, $\left[\left(1/N\right)\sum_{i=1}^{N}\left(y_{i}-x_{i}\right)^{2}\right]^{0.5}$
% wins	Percentage wins in pairwise comparisons of $y_i$ and $x_i$ from multiple models

parameters shown in Table 1 characterize the aggregate statistics based on the entire algorithm development dataset, it is also important to examine the regression models in terms of potential presence of bias at different ranges of the variable under consideration. For this purpose, we examined the patterns of the difference between the algorithm-derived and measured data across the whole range of measured values, which is similar to the Bland-Altman analysis (Altman and Bland, 1983; Bland and Altman, 1983). Overall, the consideration of statistical indicators listed in Table 1, results from pair-wise comparisons, and Bland-Altman-like plots provided a basis for selecting the final algorithm formulas presented in this study. In subsequent sections we present results for the final algorithms.

## 2.5. Design and structure of particle composition-specific algorithms

Flowcharts depicting the operational structure of particle composition-specific algorithms for estimating POC from the particulate IOPs or from remote-sensing reflectance are shown in Figs. 2 and 3, respectively. These figures also indicate the algorithm equations which are presented in subsequent sections of the paper. The IOP-based algorithms require input data of spectral  $a_{\rm p}(\lambda)$  and  $b_{\rm bp}(\lambda)$ , and the reflectance-based algorithms require input of spectral  $R_{\rm rs}(\lambda)$ . Both algorithm categories include two different methods for estimating POC, referred to as the Method-1 and Method-2 algorithms. Conceptually, the Method-1 IOP-based algorithms are similar to the Method-1  $R_{\rm rs}$ -based algorithms. Likewise, the Method-2 IOP-based algorithms are conceptually similar to the Method-2  $R_{\rm rs}$ -based algorithms.

The Method-1 algorithms consists of three main components. First, the SPM algorithm is used to estimate SPM from the input optical data. Second, the POC/SPM algorithm is used to estimate POC/SPM from the input optical data. In the final third step of Method-1 algorithms, POC is determined as a product of algorithm-derived SPM and POC/SPM. Thus, the POC derived from Method 1 accounts for changes in POC/SPM without prior classification of input optical data into particle-composition classes.

In contrast, the Method-2 algorithms do not use the SPM algorithm but require the classification of input optical data into particlecomposition classes prior to estimation of POC. First, the POC/SPM algorithm is used to estimate POC/SPM from input optical data in the same way as in Method-1. The algorithm-derived POC/SPM values are then sorted into three classes referred to as mineral-dominated with  $POC/SPM \le 0.12$ , organic-dominated with  $POC/SPM \ge 0.28$ , and mixed with POC/SPM between 0.12 and 0.28. The determination of boundary values of 0.12 and 0.28 is described in Section 2.6. The optical data that are used as input to POC/SPM algorithm are also assigned to particlecomposition classes as each algorithm-derived value of POC/SPM has its corresponding optical data. The final component of the Method-2 algorithms is calculation of POC using the algorithm formulas specific to each particle-composition class. Thus, the POC derived from Method-2 accounts for changes in POC/SPM through the use of the composition class-specific POC algorithms.

Fig. 2 also shows that each of the two methods of the IOP-based algorithms has additionally two options for determining POC. In the Method-1 algorithm the two options are associated with two separate SPM algorithms, one based on  $a_{\rm p}(\lambda)$  and the other on  $b_{\rm bp}(\lambda)$ . In the Method-2 algorithm the two options are associated with two different sets of composition class-specific POC algorithms, one set based on  $a_{\rm p}(\lambda)$  and the other on  $b_{\rm bp}(\lambda)$ . These options will be referred to as  $a_{\rm p}$ -based and  $b_{\rm bp}$ -based.

Finally, it is notable that the algorithms were formulated using the input optical data at relatively few light wavelengths which are indicated in Figs. 2 and 3. The IOP-based algorithms require  $a_{\rm p}$  at two wavelengths and  $b_{\rm bp}$  at one wavelength as these three spectral IOPs are used in the POC/SPM algorithm. The Method-1  $R_{\rm rs}$ -based algorithm requires  $R_{\rm rs}$  at three wavelengths and the Method-2 algorithm five wavelengths. The wavelengths of  $R_{\rm rs}$  depicted in Fig. 3 correspond to

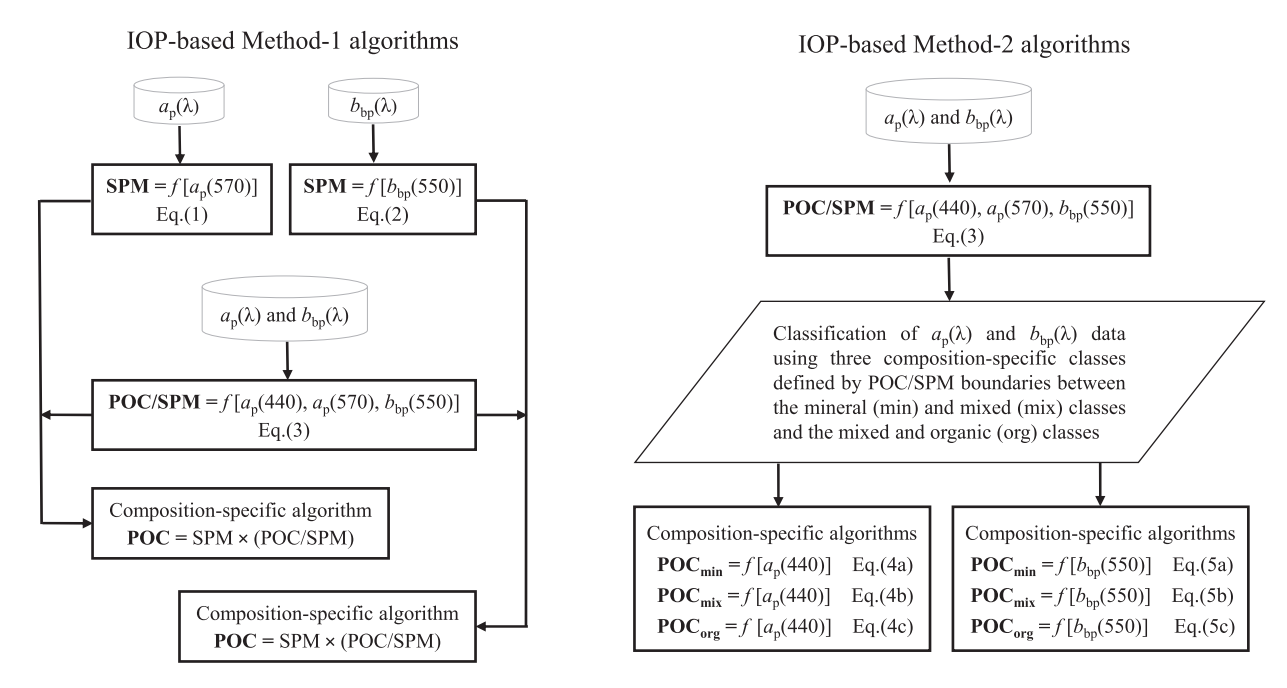


Fig. 2. Flowcharts of IOP-based Method-1 algorithms (left panel) and IOP-based Method-2 algorithms (right panel) for estimating POC. The symbol f indicates a functional relationship described by a given equation in text.

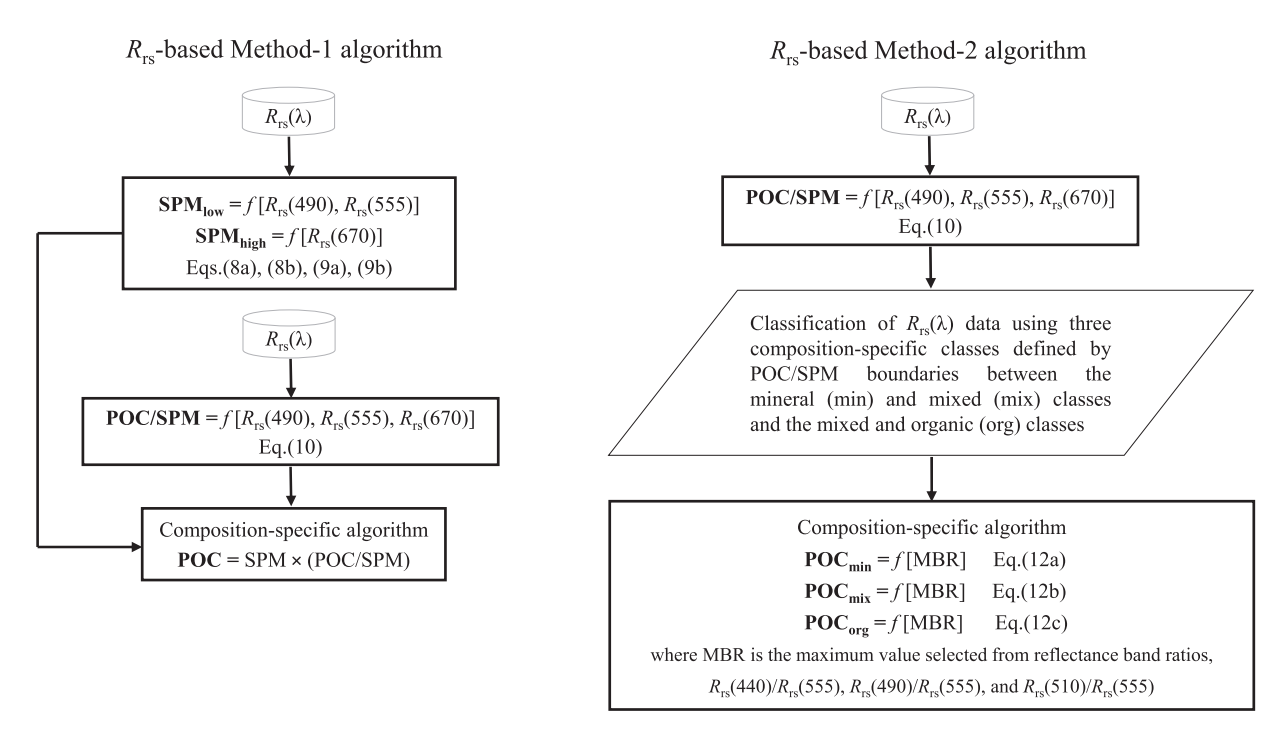


Fig. 3. Flowcharts of  $R_{rs}$ -based Method-1 algorithm (left panel) and  $R_{rs}$ -based Method-2 algorithm (right panel) for estimating POC. The symbol f indicates a functional relationship described by a given equation in text. The light wavelengths associated with remote-sensing reflectance  $R_{rs}$  correspond to nominal wavelengths of SeaWiFS spectral bands.

spectral bands of SeaWiFS (Sea-viewing Wide Field-of-View Sensor) satellite ocean color sensor. However, we also formulated analogous  $R_{\rm rs}$ -based algorithms for spectral bands available on other satellite ocean color sensors which include MODIS (Moderate Resolution Imaging Spectroradiometer on Aqua and Terra satellite missions), VIIRS-SNPP (Visible Infrared Imaging Radiometer Suite on Suomi National Polar-Orbiting Partnership mission), VIIRS-NOAA-20 (VIIRS on NOAA-20

satellite which also has been referred to as JPSS-1 for Joint Polar Satellite System mission), MERIS (MEdium Resolution Imaging Spectrometer on Envisat mission), and OLCI (Ocean and Land Colour Instrument on Sentinel-3 mission). For brevity, in the paper we present the  $R_{\rm rs}$ -based algorithms for the spectral bands of SeaWiFS. The algorithms for other sensors are provided in Supplementary Material.

## 2.6. Selecting the boundaries of particulate composition classes

As described above, the Method-2 composition-specific algorithms involve partitioning of input optical data into three particle-composition classes defined by POC/SPM and referred to as mineral-dominated, mixed, and organic-dominated. This approach is generally consistent with the study of Woźniak et al. (2010), in which the mineral-dominated class was defined as POC/SPM  $\leq$  0.06, the organic-dominated class as POC/SPM  $\geq$  0.25, and the mixed class with the POC/SPM between 0.06 and 0.25. In that study these specific criteria provided a useful means of classifying particle assemblages and interpreting associated optical measurements in near-shore waters of Southern California, and were then also used in other studies (Reynolds et al., 2016; Tran et al., 2019; Vantrepotte et al., 2012).

In the present study, we performed a correlation analysis between POC and the particulate IOPs,  $a_{\rm p}(\lambda)$  and  $b_{\rm bp}(\lambda)$  at different light wavelengths from the visible spectral region, to optimize the selection of two boundary values of POC/SPM between the composition classes, specifically the (POC/SPM)<sub>1</sub> boundary between the mineral-dominated and mixed classes and the (POC/SPM)<sub>2</sub> boundary between the mixed and organic-dominated classes. The relationships between POC and these IOPs were found particularly suitable for this analysis because changes in POC/SPM produced consistent data patterns in POC vs.  $a_{\rm p}(\lambda)$  and POC vs.  $b_{\rm bp}(\lambda)$ , which is presented in more detail in Section 3.2.

By varying (POC/SPM)<sub>1</sub> from 0.04 to 0.19 and (POC/SPM)<sub>2</sub> from 0.2 to 0.4, both with an increment of 0.01, we created 336 scenarios of compositional partitions, each having a different pair of boundary values of (POC/SPM)1 and (POC/SPM)2. In this analysis we considered data of  $a_p(\lambda)$  at seven wavelengths (420, 440, 480, 510, 555, 640 and 675 nm) and  $b_{bp}(\lambda)$  at six wavelengths (420, 442, 470, 510, 550, and 640 nm) to cover a broad portion of visible spectral region. Given the number of compositional partitioning scenarios and light wavelengths, we initially created 2352 compositionally-characterized datasets for the correlation analysis between POC and  $a_p(\lambda)$ . In these compositionallycharacterized datasets, each pair of POC and  $a_p$  measurements was classified as either mineral-dominated [if POC/SPM ≤ (POC/SPM)<sub>1</sub>], mixed [if (POC/SPM) $_1$  < POC/SPM < (POC/SPM) $_2$ ], or organicdominated [if  $POC/SPM \ge (POC/SPM)_2$ ] according to the specific pair of boundaries (POC/SPM)1 and (POC/SPM)2 associated with a given dataset. Similarly, 2016 compositionally-characterized datasets were initially created for the analysis of POC and  $b_{bp}(\lambda)$ .

To ensure a reasonable minimum sample size for correlation analysis we then disregarded the compositionally-characterized datasets which did not have at least 30 data pairs of POC and  $a_p$  or POC and  $b_{bp}$  in each compositional class. Next, for each compositionally-characterized dataset satisfying the above criteria, we calculated the Pearson correlation coefficient, R, between the log-transformed values of POC and a given IOP (i.e.,  $a_p$  or  $b_{bp}$  at specific  $\lambda$ ) for each of the three compositional classes. An average value of these three coefficients was assumed to represent a correlational score, R<sub>s</sub>, for a given compositionallycharacterized dataset. By inspecting all compositionally-characterized datasets the initial cumulative scores were then calculated for each unique pair of boundary values of (POC/SPM)1 and (POC/SPM)2 by summing the corresponding values of  $R_s$ . In the next step, the pairs of (POC/SPM)<sub>1</sub> and (POC/SPM)<sub>2</sub> values were decoupled in a sense that the final cumulative correlational score,  $R_{\rm cs}$ , for any given boundary value was obtained by summing the initial cumulative scores involving this boundary value. Finally, based on the highest  $R_{cs}$ , the optimal boundaries to delineate the three compositional classes were selected as (POC/  $SPM)_1 = 0.12$  and  $(POC/SPM)_2 = 0.28$ . We recall that this correlation analysis was performed separately for the compositionallycharacterized datasets of POC and  $a_p(\lambda)$  and the compositionallycharacterized datasets of POC and  $b_{
m bp}(\lambda)$ . It is remarkable that both analyses pointed to essentially the same optimal values of 0.11 or 0.12 for (POC/SPM)<sub>1</sub> and 0.27 or 0.28 for (POC/SPM)<sub>2</sub>.

## 3. Results and discussion

# 3.1. Concentration and composition characteristics of suspended particulate matter

The measures of pigment and particle mass concentration exhibit a broad range of variation in our field dataset that includes both the near-surface and subsurface measurements at depths extending to 300 m (Table 2). Specifically, Chla ranges from  $<\!0.01$  to over 30 mg m $^{-3}$ . The range for POC is between about 7 and 1750 mg m $^{-3}$  and for SPM from about 20 to 20,000 mg m $^{-3}$ . Using the Shapiro-Wilk test (Royston, 1995; Shapiro and Wilk, 1965), we determined that the probability distributions of POC and SPM show no substantial deviation from a log-normal distribution. The Chla distribution differs significantly from both the log-normal and normal distributions. Given a significant positive skewness of the distributions, the mean values are much greater than median values (Table 2).

The values of POC/SPM ratio vary from about 0.01 to 0.6 which covers approximately the full range that can be expected for this particulate compositional metric in natural waters (Table 2). This result indicates that the particle assemblages ranged from totally dominated by mineral particles (the lowest POC/SPM) to totally organic-dominated (the highest POC/SPM). The mean and median values of POC/SPM are nearly identical (0.255 and 0.25, respectively) but the data still exhibit a positive skewness (0.2) and are neither normally nor log-normally distributed. The examined samples are also characterized by a wide range of POC/Chla and Chla/SPM ratios (Table 2). The range of Chla/SPM is indicative of particle assemblages with highly variable contribution of phytoplankton.

Overall, the large variability in the characteristics shown in Table 2 represents diverse scenarios of both the particle concentration and composition metrics in the western Arctic seas, which range from very clear to very turbid waters with highly variable composition in terms of varying proportions of mineral, organic, phytoplankton, and non-phytoplankton particles. We recall that the dataset that includes measurements at near-surface depths and larger depths is used in this study for the analysis of relationships between particulate IOPs and particulate concentration and composition characteristics. The subset of near-surface data, which is used in this study for the analysis of  $R_{\rm rs}$ -based algorithms, is also characterized by a similarly wide range of particulate characteristics (Table 2).

## 3.2. IOP-based algorithms

## 3.2.1. SPM algorithms

The particle concentration generally exerts the first-order causal effect on IOPs of seawater. Fig. 4 illustrates data of mass concentration of suspended particulate matter, SPM, plotted as a function of particulate absorption,  $a_{\rm p}(\lambda)$ , and particulate backscattering,  $b_{\rm bp}(\lambda)$ , coefficients at example light wavelengths from the blue, green, and red spectral regions. Each data point in this figure is color coded according to a continuous scale of POC/SPM values. This provides insights into the question of potential effect of the composition of particulate matter expressed in terms of POC/SPM on the relationships between SPM and particulate IOPs.

Fig. 4 demonstrates that data points corresponding to different values of POC/SPM across the entire range of POC/SPM largely overlap and do not form separate patterns for mineral-dominated, organic-dominated, and mixed particulate assemblages. This result suggests that these particulate IOPs can provide fairly robust optical proxies for estimating SPM regardless of varying proportions of organic and mineral particles. As a result of regression analysis of several candidate functions to fit the data of SPM vs. IOPs at different wavelengths, we provide the formulas which best describe our datasets of SPM vs.  $a_p(\lambda)$  (Fig. 4b) and SPM vs.  $b_{bp}(\lambda)$  (Fig. 4e):

Table 2 Summary of characteristics of marine suspended particles in the Arctic dataset. *N* is the number of samples. The median, minimum, and maximum sampling depths for the entire dataset of concurrent SPM and POC determinations are 11.5 m, 0 m, and 300 m, respectively. For the entire dataset that includes Chla these depths are 5 m, 0 m, and 300 m. The values in parenthesis represent a subset of the entire dataset which corresponds only to near-surface measurements.

	SPM (mg m <sup>-3</sup> )	POC (mg m <sup>-3</sup> )	POC/SPM (g:g)	Chla (mg m <sup>-3</sup> )	POC/Chla (g:g)	Chla/SPM (g:g)
N	335	335	335	271	271	271
	(98)	(98)	(98)	(97)	(97)	(97)
Mean	1235.79	203.68	0.255	2.19	415.55	$1.86 \ 10^{-3}$
	(1309.54)	(182.74)	(0.307)	(1.52)	(450.65)	$(1.40 \ 10^{-3})$
Median	602.49	125.75	0.250	0.44	254.22	$8.29 \ 10^{-4}$
	(365.33)	(125.68)	(0.322)	(0.30)	(411.60)	$(7.78 \ 10^{-4})$
Minimum	23.52	6.99	0.0136	0.004	8.39	$2.74 \ 10^{-5}$
	(43.60)	(20.35)	(0.0146)	(0.025)	(32.24)	$(4.04 \ 10^{-5})$
Maximum	20,617.0	1745.92	0.583	32.76	4249.36	$3.00 \ 10^{-2}$
	(20,617.0)	(1022.13)	(0.583)	(18.10)	(1431.03)	$(0.99 \ 10^{-2})$

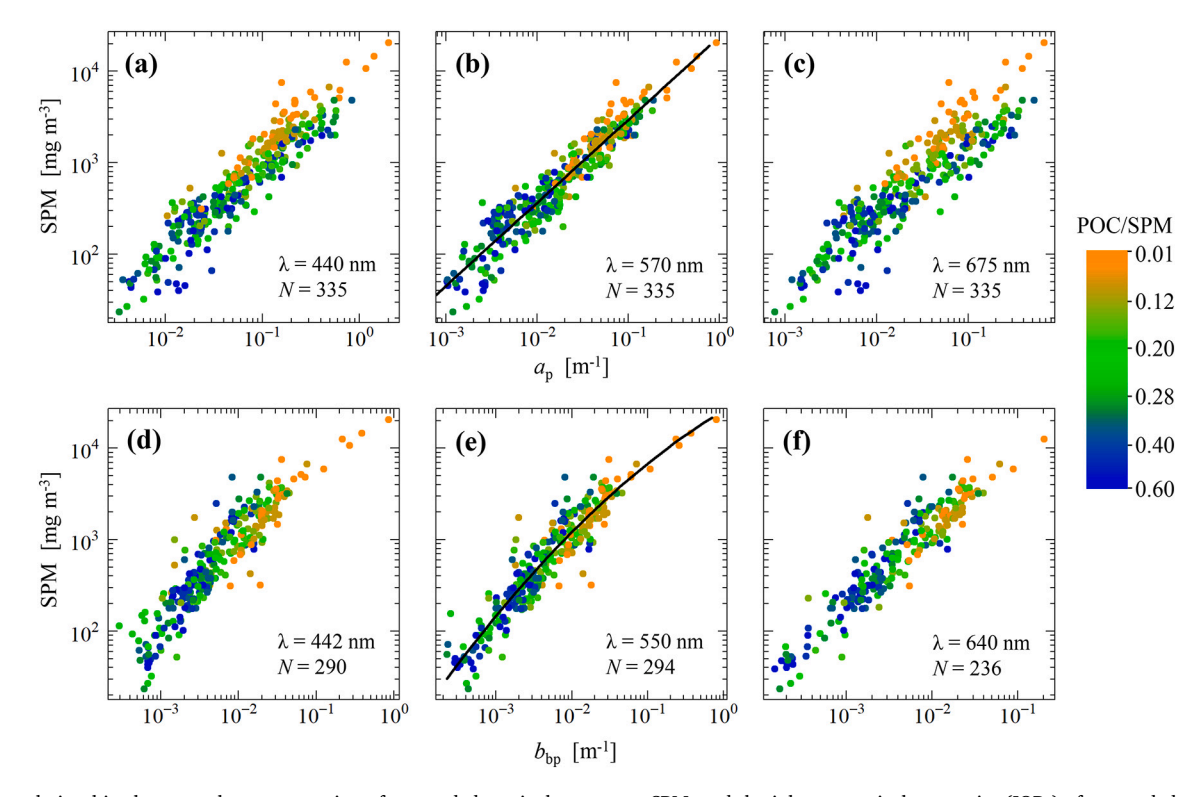


**Fig. 4.** The relationships between the concentration of suspended particulate matter, SPM, and the inherent optical properties (IOPs) of suspended particles, specifically the particulate absorption coefficient,  $a_p$ , at light wavelengths  $\lambda$  of (a) 440 nm, (b) 570 m, (c) 675 nm, as well as particulate backscattering coefficient,  $b_{\rm bp}$ , at wavelengths of (d) 442 nm, (e) 550 nm, and (f) 640 nm. Data points are color coded according to a continuum of values of particulate composition parameter, POC/SPM, as indicated in the color scale bar. The number of data (*N*) is also displayed. The best-fit regression functions representing the algorithms for estimating SPM from  $a_p$ (570) and  $b_{\rm bp}$ (550) are also shown as black lines in (b) and (e), respectively (see Section 3.2.1 for details). These regression functions represent the best fit to all data irrespective of the particulate composition parameter POC/SPM.

$$SPM = 10^{(4.37698+0.90646 A_G)}$$
 (1)

where  $A_G = log[a_p(570)]$  and

$$SPM = 10^{(4.41139 + 0.49663 B_G - 0.08396 B_G^2)}$$
 (2)

where  $B_G = \log[b_{bp}(550)]$ , the subscript "G" indicates the wavelength in the green spectral region, and log is the logarithm to base 10.

The statistical indicators describing the deviations between SPM derived from these equations and the measured SPM indicate that these algorithms provide reasonably good estimates of SPM for the algorithm development dataset (Fig. 5). For example, for SPM derived from  $a_p(570)$  the median ratio of predicted to measured values (MdR) is 0.98, and the median absolute percent difference (MdAPD) is 27.5%. Similar statistics of MdR = 1.02 and MdAPD = 24.9% were obtained for the

 $b_{
m bp}$ (550)-based algorithm. The *MdR* values indicate that an aggregate bias is very small (within 2%). We also note that the particulate IOPs measured in other spectral regions can still provide reasonably good proxies for SPM but, for our dataset, are generally not as good as those from the green spectral region. For example, compared to SPM vs.  $a_{
m p}$ (570) shown in Fig. 4b, the data points of SPM vs.  $a_{
m p}$ (675) in Fig. 4c are significantly more scattered.

# 3.2.2. Effect of particulate composition on the relationship between POC and IOPs

In contrast to results for SPM shown in Fig. 4, the relationships between POC and particulate IOPs show a clear tendency for large and fairly systematic separation of data points driven by varying POC/SPM (Fig. 6). Specifically, Fig. 6 shows that for any given POC the values of  $a_p(\lambda)$  or  $b_{bp}(\lambda)$  tend to increase with a decrease in POC/SPM. This trend

0.01

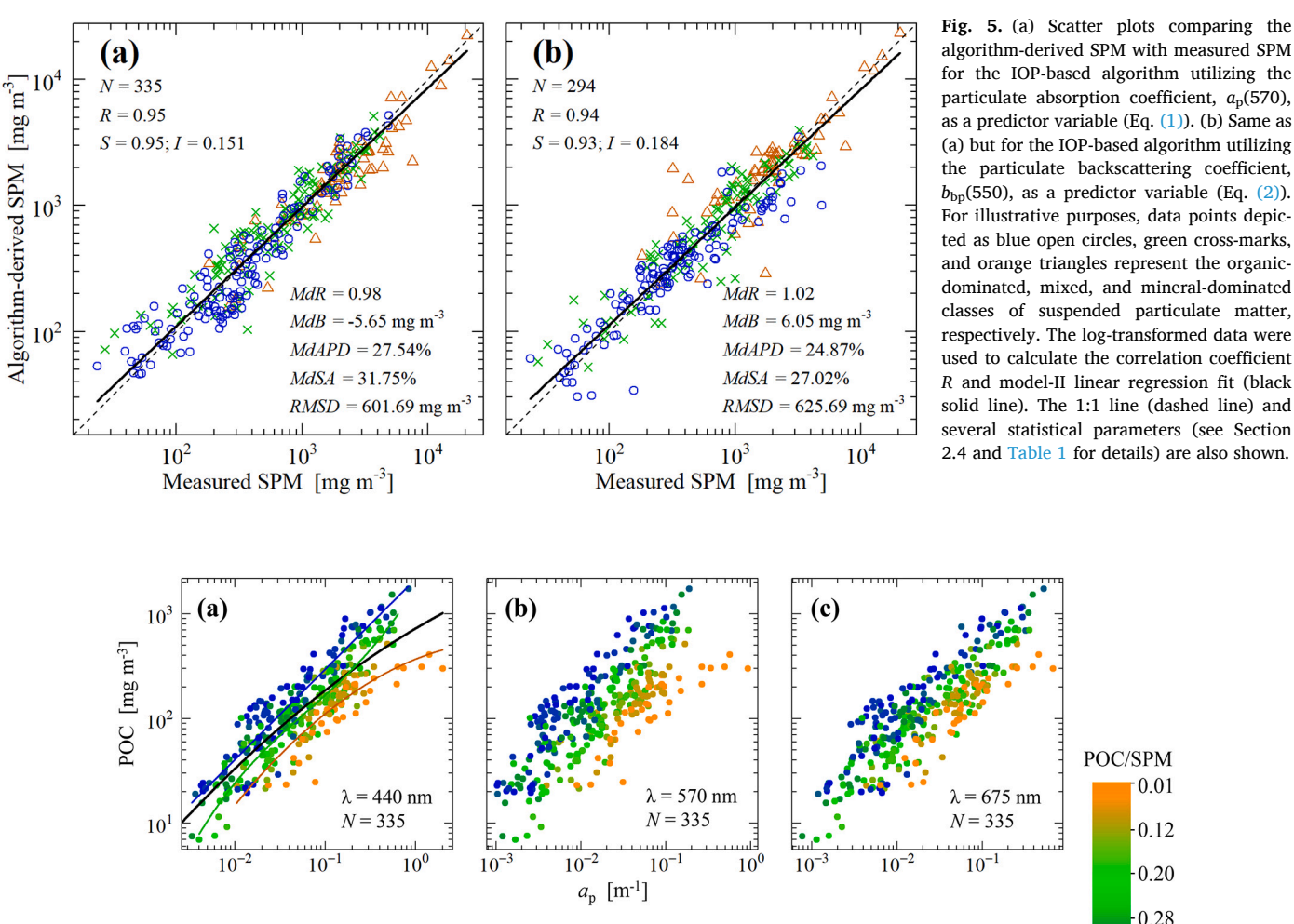
-0.12

0.20

0.28

0.40

0.60



(e)

 $10^{-3}$ 

= 442 nm

 $10^{0}$ 

= 290

 $10^{-1}$ 

 $10^{-2}$ 

Fig. 6. The relationships between the concentration of particulate organic carbon, POC, and the inherent optical properties (IOPs) of suspended particles, specifically the particulate absorption coefficient,  $a_p$ , at light wavelengths  $\lambda$  of (a) 440 nm, (b) 570 m, (c) 675 nm, as well as particulate backscattering coefficient,  $b_{bp}$ , at wavelengths of (d) 442 nm, (e) 550 nm, and (f) 640 nm. Data points are color coded according to a continuum of values of particulate composition parameter, POC/ SPM, as indicated in the color scale bar. The best-fit regression functions representing the particle-composition class-specific algorithms for estimating POC from  $a_{\rm p}(440)$  and  $b_{\rm bp}(550)$  are also shown in (a) and (e), respectively. The blue, green, and orange lines represent these best-fit functions for organic-dominated, mixed, and mineral-dominated classes of suspended particulate matter, respectively (equations are included in Section 3.2.4). For comparison, the best-fit regression functions for all data irrespective of particulate composition parameter, POC/SPM, are shown as black lines in (a) and (e). The corresponding equations are: POC =  $10^{(2.86045+0.51201\,A_{\rm B}-0.07870\,A_{\rm B}^2\,)}$  and POC =  $10^{(3.33506+0.53153\,B_{\rm G})}$  where  $A_{\rm B}=\log[a_{\rm p}(440)]$  and  $B_{\rm G}=\log[b_{\rm bp}(550)]$ .

 $10^{-2}$ 

 $b_{\rm bp}$  [m<sup>-1</sup>]

 $\lambda = 550 \text{ nm}$ 

 $10^{0}$ 

N = 294

 $10^{-1}$ 

**(f)** 

10

is readily explainable because a given value of POC represents approximately a given pool of organic particles, so an increase in the absorption and backscattering coefficients is expected with more inorganic particles (lower POC/SPM) present within the total particulate assemblage that contains a given pool of organic particles. Based on theoretical grounds governing the interactions of light with particles that have diverse physical and chemical properties (Jonasz and Fournier, 2007; Woźniak and Dera, 2007) it is not surprising that POC values at any given value of

 $10^{3}$ 

10

10

POC [mg m<sup>-3</sup>]

particulate IOP (or vice versa) can differ by more than one order of magnitude. Such large differences have been previously demonstrated with field data, for example in studies of concurrently collected measurements of POC and  $b_{\mathrm{bp}}(\lambda)$  in different regions of the Southern Ocean (Allison et al., 2010; Stramski et al., 1999) and the Pacific and Atlantic Oceans (Balch et al., 2010; Cetinić et al., 2012; Stramski et al., 2008), as well as in our earlier analyses of the Arctic data (Reynolds et al., 2016). The present results from the Arctic dataset shown in Fig. 6 provide

 $\lambda = 640 \text{ nm}$ 

 $10^{-1}$ 

N = 236

10

further evidence for such large variability associated with changes in characteristics of marine particulate assemblages. These results have also important cautionary implications for estimating POC from  $b_{\rm bp}(\lambda)$  across diverse aquatic environments (in a sense of both the geographic location and in the vertical within the water column) using the relationships that do not account for the effect of varying particulate composition. This caution is especially important in view of increased use of in situ measurements of  $b_{\rm bp}$  as a proxy of POC from a global network of Biogeochemical-Argo (BGC-Argo) profiling floats (Claustre et al., 2020; Haëntjens et al., 2017; Johnson et al., 2017; Koestner et al., 2022) as well as the use of  $b_{\rm bp}$  data product obtained from active (lidar) optical remote sensing (Behrenfeld et al., 2013; Lu et al., 2021).

Importantly, Fig. 6 suggests that while POC cannot be predicted reliably across diverse water bodies from particulate IOPs using single relationships that are indiscriminate in terms of particulate composition, improved predictions can be achieved if the effect of varying POC/SPM is accounted for in the algorithms. As described in Section 2.5, the Method-1 and Method-2 algorithms are designed to account for the effects of varying POC/SPM and specific details of such IOPs-based algorithms are presented in subsequent sections.

## 3.2.3. POC/SPM algorithm

While considering the formulation of an IOP-based algorithm for estimating the POC/SPM ratio, it is instructive to examine to what extent the mineral-dominated, mixed, and organic-dominated particle composition classes differ in terms of spectral shapes of  $a_{\rm p}(\lambda)$  and  $b_{\rm bp}(\lambda)$ . The spectral shapes of  $a_{\rm p}(\lambda)$  exhibit large variability within each compositional class although the class-specific average shapes clearly differ from one another (Fig. S1, Supplementary Material). The range of variability within each compositional class, and significant overlap between the classes, indicate that the spectral shapes of  $a_{\rm p}(\lambda)$  are unlikely to provide an efficient means for estimating POC/SPM or to discriminate between the mineral-dominated, mixed, and organic-dominated classes. Similar conclusions were drawn from the analysis of spectral shapes of  $b_{\rm bp}(\lambda)$ .

In order to formulate an empirical algorithm for estimating POC/ SPM from IOPs, we tested several formulations including the use of band ratio of  $a_p(675)/a_p(570)$  which was previously proposed as a proxy for POC/SPM on the basis of analysis of near-shore seawater samples from Southern California (Woźniak et al., 2010). For our Arctic dataset, however, this band ratio does not serve as the best predictor of POC/ SPM. Among several tested formulations, a multiple regression model involving two IOP predictors,  $a_p(570)/a_p(440)$  and  $b_{bp}(550)$ , provided the most satisfactory estimation of POC/SPM from IOPs. The  $a_{\rm p}(570)$ /  $a_{\rm p}(440)$  ratio serves to reinforce the differences between the mineraland organic-dominated particulate assemblages. As POC/SPM changes, the spectral shape of  $a_p(\lambda)$  in these spectral regions changes in opposite direction, making the green-to-blue band ratio highly sensitive to particulate composition. The second IOP predictor,  $b_{bp}(550)$ , acts as a proxy for magnitude of SPM. The graphs of POC/SPM data plotted as a function of  $a_p(570)/a_p(440)$  and  $b_{bp}(550)$  are included in Supplementary Material (Fig. S2).

The IOP-based algorithm for estimating POC/SPM as obtained from multiple regression analysis is:

$$\frac{\text{POC}}{\text{SPM}} = 10^{(-3.46591 - 4.50415 \, A_{\text{GB}} - 0.81967 \, B_{\text{G}} - 1.21707 \, A_{\text{GB}} \, B_{\text{G}})}$$
(3)

where  $A_{\rm GB} = \log[a_{\rm p}(570)/a_{\rm p}(440)]$ ,  $B_{\rm G} = \log[b_{\rm bp}(550)]$ , N = 294, and the subscripts "G" and "B" indicate the wavelengths in the green and blue spectral regions, respectively.

Fig. 7 shows the POC/SPM values predicted from Eq. (3) plotted versus measured POC/SPM. The parameters representing the aggregate statistics for the examined dataset of 294 measurements indicate that this IOP-based algorithm provides an overall good estimation of POC/SPM within our algorithm development dataset (Fig. 7). For example,

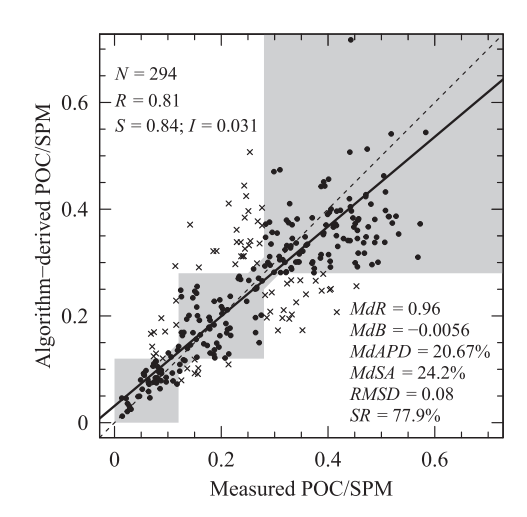


**Fig. 7.** Scatter plot comparing the algorithm-derived POC/SPM with measured POC/SPM for the IOP-based algorithm expressed by Eq. (3). The data points depicted as solid circles located within the grey shaded areas indicate that the algorithm-derived POC/SPM is correctly classified into one of the three particle-composition classes, i.e., the mineral-dominated, mixed, or organic-dominated class. The data points depicted as cross-marks outside the grey shaded areas indicate incorrect classification. The calculations of correlation coefficient *R* and model-II linear regression fit (black solid line) were made using the ordinary (untransformed) POC/SPM data. The 1:1 line (dashed line) and several statistical parameters are also shown. All data (i.e., both solid circles and crossmarks) were included in this analysis.

MdR is 0.96 and MdAPD is 20.67%.

As described in Section 2.5 and Fig. 2, the algorithm-derived POC/SPM is used directly in the estimation of POC from the Method-1 algorithms. In the Method-2 algorithms, the algorithm-derived POC/SPM is used to partition the data into three particle-composition classes; mineral-dominated, mixed, and organic-dominated. This classification is a prerequisite to development of particle-composition class-specific algorithms for estimating POC from the Method-2 algorithms.

Fig. 7 depicting data of algorithm-derived vs. measured POC/SPM illustrates explicitly which specific data of POC/SPM derived from Eq. (3) were properly classified into one of the compositional classes and which data were misclassified. The successful classification naturally corresponds to situations in which both the algorithm-derived and measured values of POC/SPM belong to the same compositional class. Specifically, when both values of POC/SPM are less or equal to 0.12 the algorithm yields successful classification into the mineral-dominated class or when both values are greater or equal to 0.28 there is a successful classification into the organic-dominated class. If both values are between these two boundaries, a successful classification into the mixed class is obtained. However, there are also situations in which the difference between the algorithm-derived and measured POC/SPM is small but these values are on both sides of boundary between the classes, i.e., either on both sides of 0.12 or 0.28. It is reasonable to consider such cases as successful classification rather than misclassification. For this purpose, we defined a margin of tolerance for the difference between the algorithm-derived and measured POC/SPM around the class boundaries. Specifically, we assumed that the classification is still successful if both POC/SPM values are on different sides of the boundary value and differ by <0.03 from one another. In Fig. 7 the three grey shaded squares including the transition areas between the squares around the class boundaries comprise the POC/SPM data that were successfully classified. The misclassified data points fall outside these grey areas.

Results of compositional classification with the IOP-based algorithm (Eq. (3)) are summarized in Table 3. The percent rate of total successful classifications (success rate *SR*) is quite high, 77.9%. The highest rate of successful classifications is obtained consistently for mineral-dominated

#### Table 3

Results of classification into the three particle-composition classes, i.e., the mineral-dominated, mixed, and organic-dominated classes, using the POC/SPM values derived from the IOP-based algorithm (left-hand side of the table, see Eq. (3) for the algorithm formula) and the  $R_{rs}$ -based algorithm (the right-hand side of the table, see Eq. (8) for the algorithm formula). The analysis of each POC/SPM algorithm is based on different number of samples (N) as indicated. The results of classification based on POC/SPM measurements serve as a reference against which the algorithm-derived classifications are compared. Each result of algorithm-derived classification includes the number of samples assigned by the algorithm to a given class followed by the percent value that describes either the rate of successful classification or the rate of failed classification. The results of successful classification are highlighted in bold font.

		IOP-based algorithm ( $N = 294$ )  Classification based on measurements			$R_{\rm rs}$ -based algorithm ( $N=98$ )		
					Classification based on measurements		
		Mineral $N = 59$	Mixed $N = 100$	Organic N = 135	Mineral $N=11$	Mixed $N=28$	Organic N = 59
Algorithm-derived classification	Mineral Mixed Organic	48; 81.4% 10; 16.9% 1; 1.7% Total successful N = 229; 77.99		0; 0% 22; 16.3% 113; 83.7%	9; 81.8% 2; 18.2% 0; 0% Total successft N = 76; 77.69	0; 0% <b>18; 64.3%</b> 10; 35.7% al classifications	0; 0% 10; 16.9% <b>49; 83.1</b> %

and organic-dominated particle assemblages. For these classes the success rates are above 80%. The misclassifications of mineral-dominated or organic-dominated assemblages are nearly always categorized as mixed particulate assemblages, which also indicates that the probability of classifying mineral-dominated sample as organic-dominated sample or vice versa is nearly zero. Perhaps not surprisingly, the success rate of classifications of mixed assemblages is lower, 68%. Most of misclassified mixed assemblages are classified as organic-dominated.

Overall, these results demonstrate that the IOP-based algorithm (Eq. (3)) has an excellent discriminatory power to distinguish between the mineral-dominated and organic-dominated particle assemblages. The discriminatory power is also very good for distinguishing the mineral-dominated from mixed assemblages. The discrimination between the mixed and organic-dominated assemblages is more challenging although the successful classification rate into the mixed class is still quite high, nearly 70%.

## 3.2.4. Particle composition-specific algorithms for estimation of POC

As described in Section 2.5 (Fig. 2), we present two methods for estimation of POC from IOP-based algorithms that account for variation in POC/SPM. In the Method-1 algorithm, POC is determined from IOPs in a straightforward manner as a product of algorithm-derived SPM (i.e., either from Eq. (1) or Eq. (2)) and the algorithm-derived POC/SPM (Eq. (3)). In the Method-2 algorithm, the POC/SPM algorithm (Eq. (3)) is first used to classify the IOP measurements into one of the three particle-composition classes, and then POC is obtained from the class-specific algorithm formulas using the classified IOPs as input.

The regression analysis applied to subsets of data satisfying the POC/SPM criteria of the three composition classes, resulted in the following particle-composition class-specific algorithms for estimating POC from  $a_p(440)$ :

$$POC_{min} = 10^{(2.56711 + 0.34418 A_B - 0.17652 A_B^2)}$$
 (4a)

$$POC_{mix} = 10^{(3.25694 + 1.44096 A_B + 0.56494 A_B^2 + 0.15640 A_B^3)}$$
(4b)

$$POC_{org} = 10^{(3.33249 + 0.86245 A_B)}$$
 (4c)

where  $A_{\rm B}=\log[a_{\rm p}(440)]$  and N is 69, 122, and 144, respectively. The class-specific formulas for estimating POC from  $b_{\rm bp}(550)$  are:

$$POC_{min} = 10^{(2.67067 + 0.20268 B_G - 0.07476 B_G^2)}$$
 (5a)

$$POC_{mix} = 10^{(4.89222 + 2.15850 B_G + 0.62190 B_G^2 + 0.09367 B_G^3)}$$
(5b)

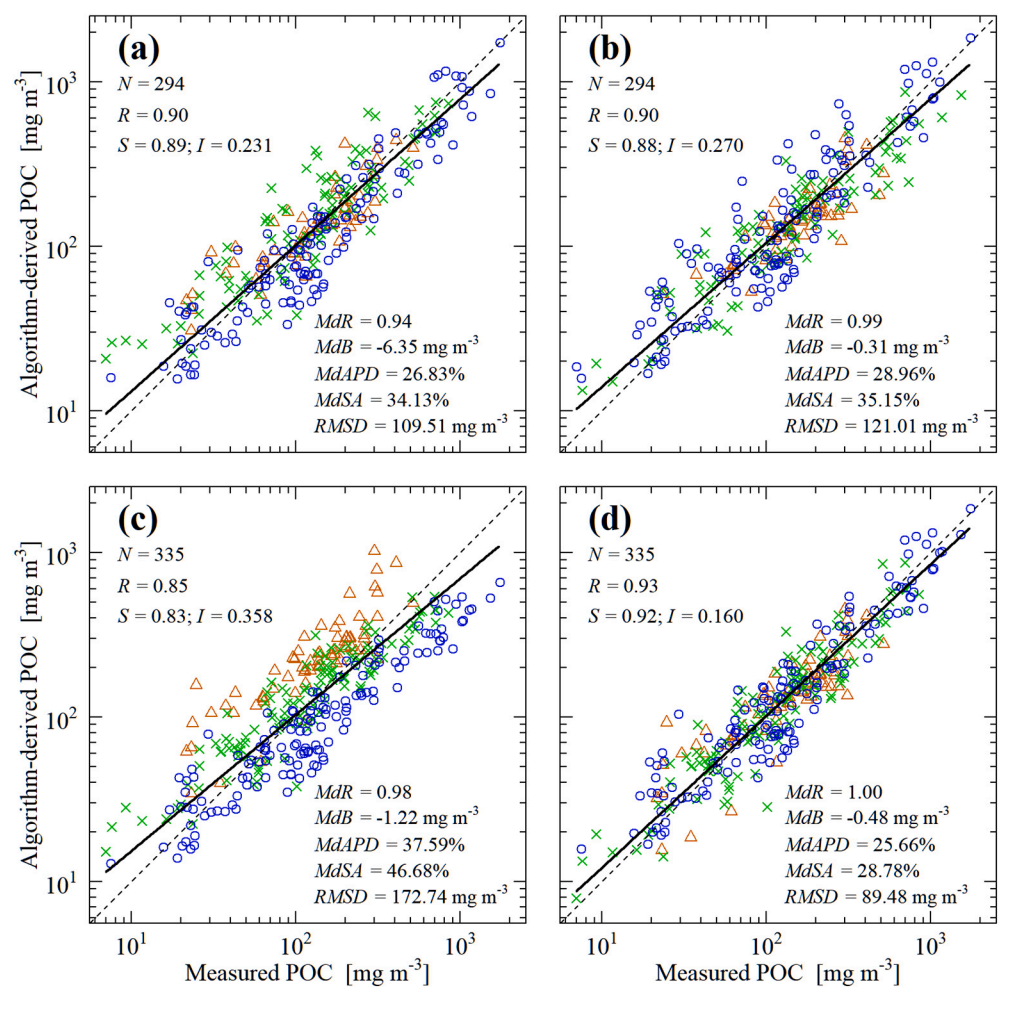
$$POC_{org} = 10^{(5.11638 + 1.27574 B_G + 0.05029 B_G^2)}$$
 (5c)

where  $B_G = \log[b_{bp}(550)]$  and N is 59, 100, and 135, respectively. The subscripts "min", "mix", and "org" indicate that POC is estimated from

class-specific formulas representative of mineral-dominated, mixed, and organic-dominated particulate classes, respectively. Note that the presented formulas involve different degrees of polynomial functions. From the analysis of several candidate formulas, we selected the functions of lowest degree beyond which there was no further improvement in goodness-of-fit statistics. The best-fit functions described by Eqs. (4) and (5) are plotted in Fig. 6a and e for the POC algorithms which use  $a_{\rm p}(440)$  and  $b_{\rm bp}(550)$ , respectively. We found that the use of  $a_{\rm p}(440)$  and  $b_{\rm bp}(550)$  for estimating POC provides generally similar or better goodness-of-fit statistics than the particulate IOPs at other wavelengths. The use of  $a_{\rm p}(440)$  and  $b_{\rm bp}(550)$  in the class-specific algorithms is advantageous because these two spectral IOPs are also involved in the POC/SPM algorithm (see Eq. (3)).

Comparisons of the algorithm-derived with measured values of POC presented in Figs. 8 and 9 provide a means to evaluate how well the different versions of IOP-based algorithms represent the main trends and variability of POC measurements within the algorithm development dataset. Fig. 8a and b illustrate such evaluation of  $a_p$ -based Method-1 and Method-2 algorithms, respectively. We recall that these algorithms are referred to as  $a_p$ -based because SPM is estimated from  $a_p(570)$ in the Method-1 algorithm (Eq. (1)), and the class-specific formulas use  $a_{\rm p}(440)$  in the Method-2 algorithm (Eq. (4)). We recall, however, that the backscattering coefficient is also used in  $a_p$ -based algorithms (both Method-1 and Method-2) because the estimation of POC/SPM requires the input of  $b_{\rm bp}(550)$  in addition to  $a_{\rm p}(440)$  (Eq. (3)). As shown in Fig. 8a and b and the statistical parameters included therein, the Method-1 and Method-2 algorithms offer similar performance based on the analysis of the algorithm development dataset. Both algorithms represent well the main trend of POC within most of the POC dynamic range. The exceptions are observed at the lowest and highest POC where the algorithms tend to overestimate and underestimate POC, respectively. Overall, given a broad range of particulate composition in the dataset, the aggregate statistical metrics for both Method-1 and Method-2 particle composition-specific algorithms are reasonably good, for example MdAPD is below 30%.

Fig. 8c provides an important comparative result because it demonstrates the extent to which the estimation of POC deteriorates when POC is calculated from a single general formula obtained by fitting the regression function to all data of POC vs.  $a_p(440)$  shown in Fig. 6a regardless of variations in POC/SPM (note that this general fit and corresponding formula are included in Fig. 6). Compared with Fig. 8a and b, Fig. 8c exhibits inferior statistical parameters, especially in terms of worsening *RMSD*, *MdAPD*, and *MdSA*. In addition, the deviations between the linear fit and the 1:1 line indicates that the general algorithm has stronger tendency for bias in estimated POC at both ends of POC range (Fig. 8c) compared with the particle composition-specific algorithms (Fig. 8a and b). Overall, the results in Fig. 8a, b, and c demonstrate the potential for significant improvements of POC



8. Scatter plots comparing the algorithm-derived POC with measured POC for different variants of absorption-based algorithms: Method-1 (a) composition-specific algorithm utilizing Eq. (1) and Eq. (3) for calculating POC, (b) Method-2 particle composition-specific algorithm utilizing Eq. (3) for POC/SPM-based classification and Eq. (4a), (4b), (4c) for calculating POC from class-specific formulas, (c) general best-fit regression function utilizing  $a_p(440)$  as a predictor variable irrespective of POC/SPM (see black line in Fig. 6a), and (d) similar to (b) but POC/SPMbased classification was made using the measured values of POC/SPM instead of Eq. (3). For illustrative purposes, data points depicted as blue open circles, green crossmarks, and orange triangles represent the organic-dominated, mixed, and mineraldominated classes of suspended particulate matter, respectively. The log-transformed data were used to calculate the correlation coefficient R and model-II linear regression fit (black solid line). The 1:1 line (dashed line) and several statistical parameters are also shown.

estimation from both the Method-1 and Method-2 particle compositionspecific algorithms compared to general algorithm that does not account for variations in POC/SPM.

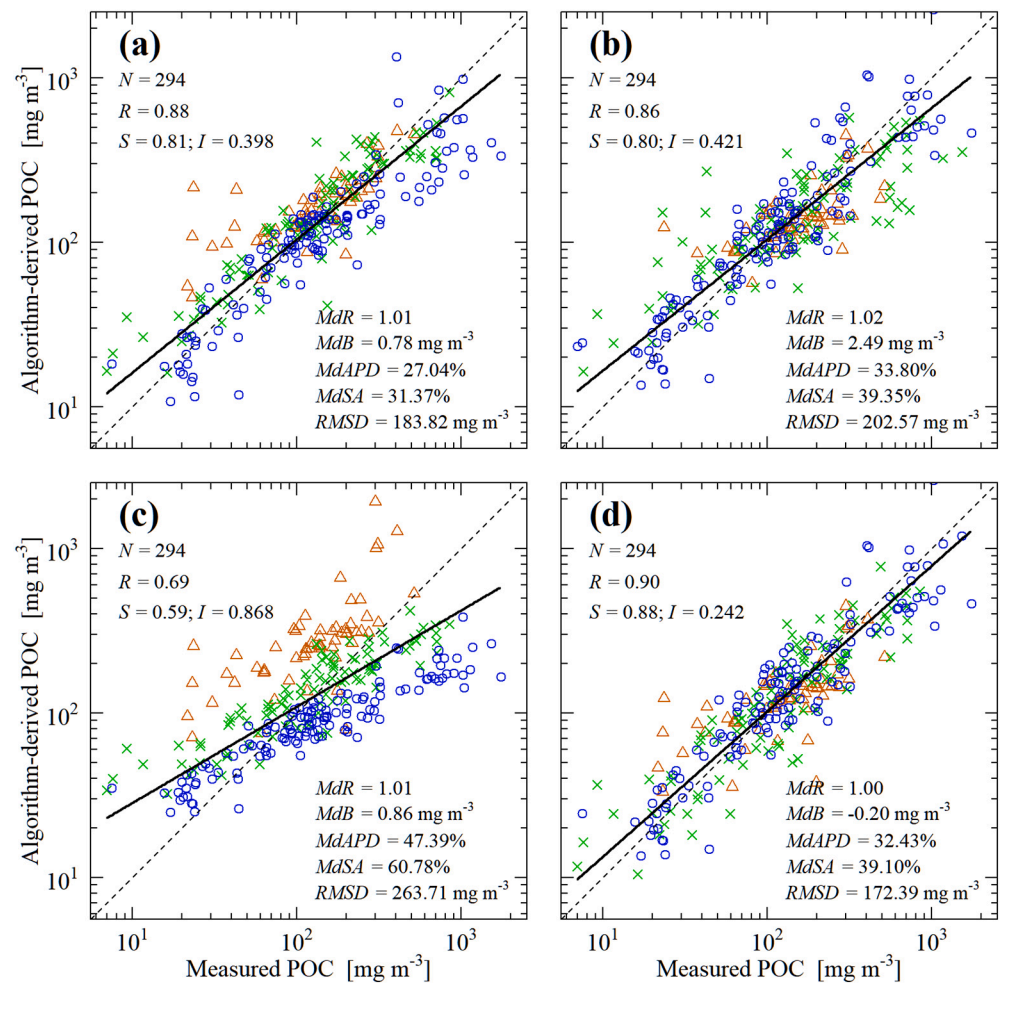
Fig. 8d is intended for comparison with Fig. 8b to provide additional insight into performance of the Method-2 algorithm that involves the classification of data into the three particle-composition classes. Whereas Fig. 8b represents the actual operational scenario of Method-2 algorithm that relies totally on input data of optical measurements, Fig. 8d shows results in which the classification of input data entering the class-specific formulas for estimating POC (Eqs. (4a), (4b), (4c)) was made using the measured values of POC/SPM rather than algorithmderived POC/SPM from Eq. (3). Thus, the results in Fig. 8d are free of misclassification errors which affect to a certain degree the operational performance of Method-2 algorithm. As expected, the statistical parameters in Fig. 8d are somewhat improved compared to Fig. 8b, especially RMSD, MdSA, and the closeness of the linear fit to the 1:1 line at low and high POC values. Although the results in Fig. 8d were obtained by skipping the optically-based estimation of POC/SPM (i.e., assuming that this parameter is known a priori) and thus do not represent the full optically-based operational scenario of Method-2 algorithm, they provide additional support for the concept of class-specific algorithms.

Analogous to Fig. 8, results for the  $b_{\rm bp}$ -based POC algorithms are depicted in Fig. 9. The main conclusions from the analysis of  $b_{\rm bp}$ -based algorithms are qualitatively consistent with those for the  $a_{\rm p}$ -based algorithms. However, the statistics for the  $b_{\rm bp}$ -based algorithms are generally inferior compared with the statistics for the  $a_{\rm p}$ -based algorithms, which is especially evident when the RMSD values are compared.

It is important to note that although the proposed IOP-based approach has no immediate applicability in conjunction with passive remote sensing of ocean color or active lidar-based optical remote sensing, it does have the potential for such applications in the future. Significant research efforts have been and continue to be devoted to algorithms for IOP retrieval from satellite observations of ocean reflectance (Jorge et al., 2021; Lee et al., 2002; Loisel et al., 2018; Loisel and Stramski, 2000; Werdell et al., 2013). While  $b_{bp}(\lambda)$  has been among the IOPs retrieved from ocean reflectance obtained from both passive and active optical remote sensing (Behrenfeld et al., 2013; Werdell et al., 2018), the retrievals of  $a_p(\lambda)$  have not yet been demonstrated and validated. Nevertheless, this capability appears attainable, especially with further advances in models that aim at partitioning the total absorption coefficient of seawater, which is derivable from ocean reflectance, into particulate and non-particulate absorption components (Stramski et al., 2019; Zhang et al., 2015; Zheng and Stramski, 2013). Such advances can provide a foundation for future implementation of the IOP-based approach for estimating POC/SPM and POC from optical remote sensing observations.

# 3.3. Reflectance-based algorithms

Linking the characteristics of particulate assemblages such as SPM, POC/SPM, and POC to particulate IOPs (as described in Section 3.2) has robust mechanistic basis in a sense that all variables involved in the examined relationships pertain strictly to particles suspended in water. In the context of optical remote sensing, the most common approach to estimate the particulate characteristics has been to use direct empirical



9. Scatter plots comparing the algorithm-derived POC with measured POC for different variants of backscattering-based algorithms: Method-1 (a) composition-specific algorithm utilizing Eq. (2) and Eq. (3) for calculating POC, (b) Method-2 particle composition-specific algorithm utilizing Eq. (3) for POC/SPM-based classification and Eq. (5a), (5b), (5c) for calculating POC from class-specific formulas, (c) general best-fit regression function utilizing  $b_{\rm bp}(550)$  as a predictor variable irrespective of POC/SPM (see black line in Fig. 6e), and (d) similar to (b) but POC/SPMbased classification was made using the measured values of POC/SPM instead of Eq. (3). For illustrative purposes, data points depicted as blue open circles, green crossmarks, and orange triangles represent the organic-dominated, mixed, and mineraldominated classes of suspended particulate matter, respectively. The log-transformed data were used to calculate the correlation coefficient R and model-II linear regression fit (black solid line). The 1:1 line (dashed line) and several statistical parameters are also shown.

relationships between the spectral remote-sensing reflectance,  $R_{rs}(\lambda)$ , and particulate characteristics of interest. Apart from the fact that  $R_{rs}(\lambda)$  is an AOP rather than IOP, this approach is limited from a mechanistic standpoint because, in addition to suspended particles, chromophoric dissolved organic matter (CDOM) can contribute significantly to variability in  $R_{rs}(\lambda)$ . These effects are typically most pronounced in the UV and short-wavelength portion of the visible spectrum where the CDOM

absorption coefficient,  $a_{\rm g}(\lambda)$ , makes large or dominant contribution to light absorption (Babin et al., 2003b; Nelson and Siegel, 2013). It is thus instructive to inspect the patterns of variability in concurrent measurements of  $a_{\rm g}(\lambda)$  and particle concentration metrics for the surface samples from our Arctic dataset (Fig. 10). Specifically, we show the scatter plots of  $a_{\rm g}(412)/{\rm POC}$  and  $a_{\rm g}(412)/{\rm Chla}$  as a function of SPM, which illustrate the patterns in CDOM absorption relative to POC or Chla

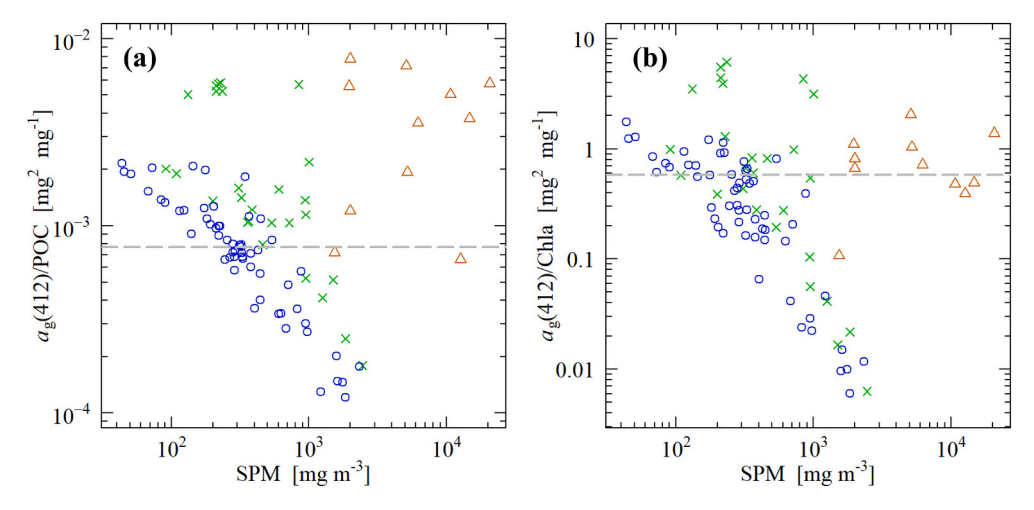


Fig. 10. (a) The ratio of the CDOM absorption coefficient at 412 nm to POC,  $a_g(412)$ / POC, as a function of SPM. (b) Same as (a) but for the ratio  $a_g(412)$ /Chla. Only data for near-surface samples which were used in the development of Rrs-based algorithms are presented (N = 96 for  $a_o(412)/POC$  and N =95 for  $a_o(412)$ /Chla). For illustrative purposes, data points depicted as blue open circles, green cross-marks, and orange triangles represent the organic-dominated, mixed, and mineral-dominated classes of suspended particulate matter, respectively. The dashed horizontal lines depict the values of  $a_0(412)/POC = 0.00077 \text{ m}^2/\text{mg}$ and  $a_g(412)$ /Chla = 0.581 m<sup>2</sup>/mg. These values represent the upper boundary of data included in recent assembly of global POC algorithm development dataset intended to be representative primarily of open-ocean pelagic environments (Stramski et al., 2022).

as the particle concentration in water varies. We note that the two ratios,  $a_g(412)/POC$  and  $a_g(412)/Chla$ , were recently included in the set of criteria for assembling a global field dataset in support of development of global POC algorithms for different satellite ocean color sensors (Stramski et al., 2022). In this recent study, only data with  $a_g(412)/POC$  $\leq 0.00077 \text{ m}^2/\text{mg C}$  and  $a_g(412)/\text{Chla} \leq 0.581 \text{ m}^2/\text{mg Chla}$  were included in the global algorithm development dataset that was intended to be representative primarily of open-ocean pelagic environments. In the present Arctic dataset, the data are both below and above these threshold values (Fig. 10), which indicates a much broader range of variability in CDOM absorption relative to particulate characteristics than typically observed in ocean pelagic environments. In addition, Fig. 10 shows that the Arctic waters with organic-dominated particulate assemblages, and to large degree also waters with mixed particulate assemblages, exhibit a clear trend of decreasing CDOM absorption relative to POC and Chla as the particle concentration SPM increases. No such trend is observed for waters with mineral-dominated particulate assemblages.

In the following Sections 3.3.1, 3.3.2 and 3.3.3 we describe the analysis of the Arctic dataset to formulate algorithms for estimating SPM, POC/SPM, and POC from  $R_{\rm rs}(\lambda)$  measured in spectral bands available on SeaWiFS satellite ocean color sensor. Analogous algorithms based on sensor-specific spectral bands available on other satellite sensors (i.e., MODIS, VIIRS, MERIS, and OLCI) are described in Supplementary Material.

## 3.3.1. SPM algorithms

The algorithms for estimating SPM in surface waters of aquatic environments from measurements of  $R_{rs}(\lambda)$  using spectral bands in the VIS and NIR spectral regions have been extensively explored in the past (e.g., Doxaran et al., 2002, 2012; Nechad et al., 2010; Siswanto et al., 2011; Han et al., 2016; Wei et al., 2021). Several studies demonstrated that the relationships between SPM and  $R_{rs}(\lambda)$  measured at a single waveband or combination of wavebands from the red and NIR spectral regions can provide a relatively simple and effective algorithm (e.g., Hu et al., 2004; Miller and McKee, 2004; Ouillon et al., 2008; Nechad et al., 2010; Ondrusek et al., 2012; Han et al., 2016; Novoa et al., 2017). We determined that a third-degree polynomial function between the log-transformed variables of SPM and  $R_{\rm rs}$  in the red spectral band provides good representation of the Arctic dataset over the entire range of measured SPM from about 20 to over 20,000 mg m<sup>-3</sup> (Fig. 11a, grey line). Although this single formula provides a good fit to our field data over the entire range of SPM and the use of the red band minimizes CDOM effects, the performance of such algorithm with satellite observations is expected to decline with a decrease in particle concentration as  $R_{rs}$  in the red spectral region becomes very low. As shown in Fig. 11a,  $R_{\rm rs}(670)$  is generally less than about 0.001 sr<sup>-1</sup> when SPM is <2000 mg m<sup>-3</sup> and decreases to values below 0.0001 sr<sup>-1</sup> in very clear waters where SPM can be <100 mg m $^{-3}$ . Another potential challenge in the context of algorithm application to satellite observations in clear waters is that satellite-derived  $R_{rs}$  in the red spectral region may be subject to significant relative bias (Bisson et al., 2021).

To circumvent these potential limitations, we formulated the hybrid SPM algorithm which consists of two empirical formulas based on the Arctic dataset. Specifically, at low  $R_{\rm rs}(670) < 0.0008~{\rm sr}^{-1}$  corresponding to SPM approximately <2000 mg m $^{-3}$  (for convenience referred to as low SPM waters), the algorithm for estimating SPM<sub>low</sub> is based on the green-to-blue band ratio of reflectance. For  $R_{\rm rs}(670) > 0.0012~{\rm sr}^{-1}$  corresponding to higher SPM (referred to as high SPM waters), our hybrid algorithm for estimating SPM<sub>high</sub> uses the single red band. The best-fit regression functions for SeaWiFS bands are:

$$SPM_{low} = 10^{\left[2.93073 + 1.80878 \, R_{G/B} - 0.87138 \, \left(R_{G/B}\right)^2\right]} \tag{6a}$$

$$SPM_{high} = 10^{\left[6.57007 + 1.56050 R_R + 0.13979 (R_R)^2\right]}$$
 (6b)

where  $R_{\rm G/B}=\log[R_{\rm rs}({\rm G})/R_{\rm rs}({\rm B})],\ R_{\rm R}=\log[R_{\rm rs}({\rm R})],\ {\rm and}\ R_{\rm rs}({\rm B}),\ R_{\rm rs}({\rm G})$  and  $R_{\rm rs}({\rm R})$  are measured in the blue (B), green (G), and red (R) spectral bands. For SeaWiFS, these bands are centered at 490, 555, and 670 nm, respectively. The formula for SPM<sub>low</sub> represents the best-fit to data which satisfied the condition  $R_{\rm rs}({\rm R})<0.0012\ {\rm sr}^{-1}\ (N=87,\ {\rm Fig.}\ 11{\rm b}).$  The formula for SPM<sub>high</sub> was obtained using data with  $R_{\rm rs}({\rm R})>0.0008\ {\rm sr}^{-1}\ (N=16,\ {\rm Fig.}\ 11{\rm a},\ {\rm solid}\ {\rm black}\ {\rm line}).$  We note that within this range of  $R_{\rm rs}({\rm R})$ , the SPM<sub>high</sub> function in Eq. (6b) is consistent with the third-degree polynomial function that was fitted to the entire dataset (Fig. 11a, grey line). A weighting approach is applied to both formulas of the hybrid algorithm in the transition range  $0.0008 \le R_{\rm rs}({\rm R}) \le 0.0012\ {\rm sr}^{-1}$ :

$$SPM = w SPM_{low} + (1-w) SPM_{high}$$
 (7a)

$$w = 0.5 + 0.5 \cos\left(\frac{\pi \left[R_{\rm rs}(R) - 0.0008\right]}{0.0004}\right)$$
 (7b)

where the argument of the cosine function is expressed in radians. The weighting function w decreases from 1 to 0 with an increase in  $R_{\rm rs}(R)$  from 0.0008 to 0.0012 sr<sup>-1</sup>, and ensures a smooth transition near the boundaries of the transition region. A similar approach for SPM algorithm using such boundaries within the dynamic range of reflectance was recently proposed by Wei et al. (2021).

The SPM hybrid algorithm described by Eqs. (6) and (7) provides generally good agreement between the algorithm-derived and measured SPM, for example MdR is 0.96 and MdAPD is 20.66% (Fig. 11c). Similar SPM algorithms for the MODIS, VIIRS, MERIS, and OLCI sensors utilize the reflectances  $R_{\rm rs}(B)$ ,  $R_{\rm rs}(G)$ , and  $R_{\rm rs}(R)$  at sensor-specific spectral bands closest to those on SeaWiFS (Table S1, Supplementary Material). The associated statistical parameters characterizing the goodness-of-fit of sensor-specific SPM algorithms are given in Table S2 (Supplementary Material).

## 3.3.2. POC/SPM algorithms

In the Arctic dataset the spectral shapes of  $R_{\rm rs}(\lambda)$  exhibit significant overlap between the particle-composition classes although the average spectral shape for mineral-dominated class is clearly different from the organic-dominated and mixed classes (Fig. S3, Supplementary Material). The organic-dominated and mixed classes, however, show no significant difference in average spectral shape of  $R_{\rm rs}(\lambda)$ . This result indicates potential limitations of the optical water type classification based on the spectral shape of  $R_{\rm rs}(\lambda)$  to differentiate water bodies that differ in terms of particulate composition parameterized with POC/SPM.

In order to formulate the  $R_{\rm rs}$ -based algorithm for estimating POC/SPM we examined the concurrent POC/SPM and  $R_{\rm rs}(\lambda)$  measurements and found that a multiple regression model involving three reflectance predictors spanning the spectral range from the blue through the red bands provides a reasonably good algorithm. The best-fit algorithm formula utilizing the blue, green and red bands of SeaWiFS is:

$$\frac{\text{POC}}{\text{SPM}} = 10^{(-3.58449 - 1.08487 \, R_{\text{B}} - 0.52062 \, R_{\text{B}} \, R_{\text{G}} + 0.43186 \, R_{\text{B}} \, R_{\text{R}})}$$
(8)

where  $R_{\rm B}=\log[R_{\rm rs}(490)]$ ,  $R_{\rm G}=\log[R_{\rm rs}(555)]$ ,  $R_{\rm R}=\log[R_{\rm rs}(670)]$ , and N=98. Similar POC/SPM algorithms for the MODIS, VIIRS, MERIS, and OLCI sensors are presented in Table S3 (Supplementary Material). Also, the data of POC/SPM plotted as a function of  $R_{\rm rs}(490)$ ,  $R_{\rm rs}(555)$ , and  $R_{\rm rs}(670)$  are shown in Fig. S4 (Supplementary Material).

Fig. 12 shows that POC/SPM derived from Eq. (8) agrees generally well with measured POC/SPM, for example MdR is virtually 1 and MdAPD is 21.65%. As the estimation of POC/SPM from this  $R_{rs}$ -based algorithm provides a means to classify the particulate assemblages into the three particle-composition classes, Fig. 12 also illustrates which specific data of algorithm-derived POC/SPM were properly classified and which data were misclassified. The same criteria for successful classification were applied as described in Section 3.2.3 in relation to the

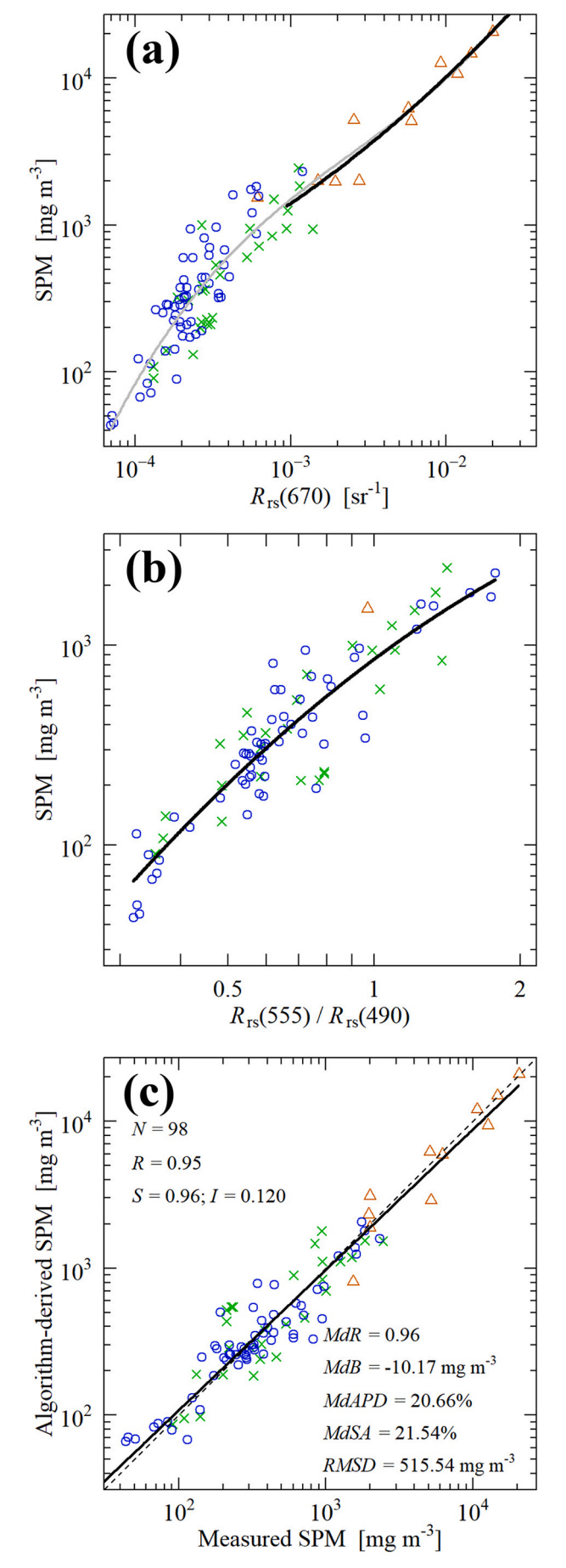


Fig. 11. (a) The relationship between SPM and remote-sensing reflectance in the red spectral band,  $R_{rs}$  (670). The solid black line is the best-fit regression function representing the SPM<sub>biob</sub> component of the hybrid algorithm for estimating SPM from remote-sensing reflectance (Eq. (6b)). For comparison, the grey line is the best-fit regression function over the entire range of data. This function is:  $\log(\text{SPM}) = a + b \log[R_{rs}(670)] + c \log[R_{rs}(670)]^2 + d \log[R_{rs}(670)]^3$  where a = 8.71184, b = 4.47426, c = 1.42229, and d = 0.18204. (b) The relationship between SPM and the spectral band ratio of remote-sensing reflectance,  $R_{\rm rs}(555)/R_{\rm rs}(490)$ . The solid black line is the best-fit regression function representing the  $\ensuremath{\mathsf{SPM}_{\mathsf{low}}}$  component of the hybrid algorithm for estimating SPM from remote-sensing reflectance (Eq. (6a)). (c) Scatter plot comparing SPM derived from the hybrid algorithm (Eqs. (6a), (6b), (7a), (7b)) with measured SPM. The log-transformed data were used to calculate the correlation coefficient R and model-II linear regression fit (black solid line). The 1:1 line (dashed line) and several statistical parameters are also shown in (c). Only data for near-surface samples (N = 98) used in the development of  $R_{rs}$ -based algorithms are presented in this figure and, for illustrative purposes, data points depicted as blue open circles, green cross-marks, and orange triangles represent the organicdominated, mixed, and mineral-dominated classes of suspended particulate matter, respectively. The presented regression functions in (a) and (b) represent the best fit to all data irrespective of the particulate composition parameter POC/SPM.

IOP-based algorithm. The results of compositional classification of the  $R_{rs}$ -based algorithm are summarized in Table 3 which also shows similar results for the IOP-based algorithm discussed in Section 3.2.3. Although the size of the development dataset of  $R_{rs}$ -based algorithm is much smaller than that for IOP-based algorithm (i.e., N = 98 vs. N = 294), the patterns of successful classification and misclassifications are similar for both types of algorithms. For example, the rate of total successful classifications is essentially the same and quite high, i.e., 77.6% for the  $R_{\rm rs}$ based algorithm vs. 77.9% for the IOP-based algorithm. Also, the highest rates of successful classifications (>80%) are obtained for mineraldominated and organic-dominated particulate assemblages and the misclassifications of mineral-dominated or organic-dominated assemblages are always categorized as mixed assemblages. The success rate of classifications of mixed particle assemblages is somewhat lower for the  $R_{\rm rs}$ -based algorithm (64.3%) than the IOP-based algorithm (68%) and most of misclassified mixed assemblages are classified as organic-

Overall, the  $R_{\rm rs}$ -based algorithm for estimating POC/SPM (Eq. (8)) has an excellent discriminatory power to distinguish between the mineral-dominated and organic-dominated particle assemblages. The algorithm also distinguishes well the mineral-dominated from mixed assemblages. The discrimination between the mixed and organic-dominated assemblages is not as good but the successful classification rates into the mixed class are still nearly 65%. The statistical parameters characterizing the goodness-of-fit and success rate of classification of other ocean color sensor-specific  $R_{\rm rs}$ -based algorithms for estimating POC/SPM are given in Table S4 (Supplementary Material).

# $3.3.3. \ \ Particle\ composition-specific\ algorithms\ for\ estimation\ of\ POC$

Similar to IOP-based algorithms, we present two methods for estimation of POC from  $R_{\rm rs}$ -based algorithms that account for variation in POC/SPM (see Section 2.5 and Fig. 3). In the Method-1 algorithm, POC is determined from  $R_{\rm rs}$  in a straightforward manner as a product of algorithm-derived SPM (Eqs. (6) and (7)) and the algorithm-derived POC/SPM (Eq. (8)). The goodness-of-fit parameters for ocean color sensor-specific Method-1 POC algorithms as obtained from the analysis of algorithm-derived vs. measured POC, are given in Table S5 (Supplementary Material). In the Method-2 algorithm, the POC/SPM algorithm (Eq. (8)) is first used to classify the  $R_{\rm rs}$  measurements into the particle-composition classes, and then POC is obtained from the class-specific algorithm formulas using the classified  $R_{\rm rs}$  data as input.

Fig. 13a depicts the Arctic data of POC vs. MBR (maximum band ratio) where MBR is the highest value selected from the three reflectance

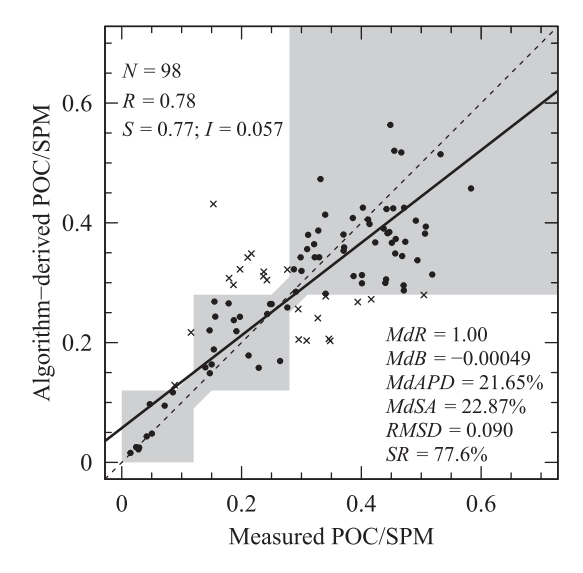


**Fig. 12.** Scatter plot comparing the algorithm-derived POC/SPM with measured POC/SPM for the  $R_{\rm rs}$ -based algorithm expressed by Eq. (8). The data points depicted as solid circles located within the grey shaded areas indicate that the algorithm-derived POC/SPM is correctly classified into one of the three particulate compositional classes, i.e., the mineral-dominated, mixed, or organic-dominated class. The data points depicted as cross-marks indicate incorrect classification. The calculations of correlation coefficient R and model-II linear regression fit (black solid line) were made using the ordinary (untransformed) POC/SPM data. The 1:1 line (dashed line) and several statistical parameters are also shown. All data (i.e., both solid circles and cross-marks) were included in this analysis.

band ratios which are  $R_{\rm rs}(443)/R_{\rm rs}(555)$ ,  $R_{\rm rs}(490)/R_{\rm rs}(555)$ , and  $R_{\rm rs}(510)/R_{\rm rs}(555)$  for SeaWiFS. The presented data are color coded according to assignment to one of the three particle-composition classes which suggests that the relationship between POC and MBR can be improved when data classified into organic-dominated and mixed particulate assemblages are analyzed separately. Importantly, these two classes of data cover a broad dynamic range in POC and MBR and are quite well separated from each other with organic-dominated assemblages exhibiting generally higher POC at any given value of MBR. The

relationship for the mineral-dominated class is inherently weaker and more difficult to establish because POC-bearing particles represent only a small fraction of the whole particulate assemblage that affects MBR. In our analysis, this difficulty is exacerbated by a small number of matchup measurements of POC and  $R_{\rm rs}(\lambda)$  for the mineral-dominated class and a relatively small dynamic range of these data in the Arctic dataset. Nevertheless, we determined the best-fit regression function for the mineral-dominated class in addition to the best-fitting regression models for the organic-dominated and mixed classes. The formulas of these  $R_{\rm rs}$ -based particle-composition class-specific algorithms are:

$$POC_{org} = 10^{[2.57147 - 2.25381 \log(MBR)]}$$
 (9a)

$$POC_{mix} = 10^{[2.19029 - 1.78080 \log(MBR)]}$$
 (9b)

$$POC_{min} = 10^{[2.27703 - 0.84220 \log(MBR)]}$$
 (9c)

where the number of observations is 59, 28, and 11 for the organic-dominated (org), mixed (mix), and mineral-dominated (min) classes, and MBR is based on SeaWiFS bands as indicated above. In this analysis of composition-specific subsets of data, we found no statistical justification for using higher degree polynomials than the first-degree polynomial. The best-fit functions corresponding to Eqs. (9a), (9b), and (9c) are depicted in Fig. 13a. Analogous class-specific algorithms for estimating POC from  $R_{rs}(\lambda)$  for other ocean color sensors and associated goodness-of-fit statistical parameters are presented in Table S6 and S7 (Supplementary Material).

For comparison, Fig. 13a also includes the best-fit function (black solid line) to all data regardless of POC/SPM. Many data points deviate greatly from this function indicating that such indiscriminate approach has high uncertainty and can often produce large errors when applied across wide range of particulate compositions. However, because one of our motivations to develop and demonstrate the particle composition-specific algorithms in this study is to stimulate further advancements of this approach towards its broader applicability across diverse environments beyond specific regional limits, it is of more interest for comparative analysis to illustrate how the current standard global POC algorithm performs with our Arctic data that covers a broad range of particulate compositions. To this end, Fig. 13b depicts our field data of POC vs.  $R_{\rm rs}(443)/R_{\rm rs}(555)$  along with the line representing the current

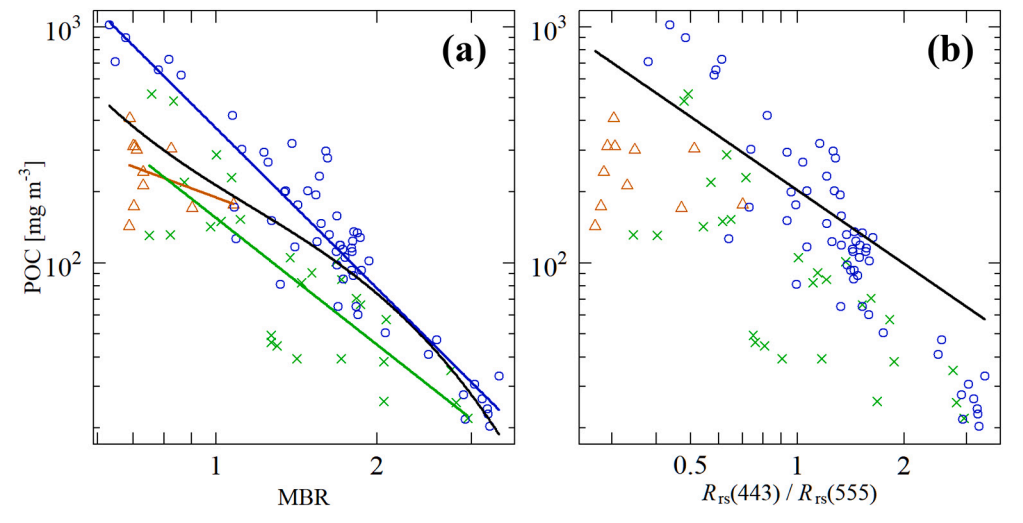


Fig. 13. (a) The relationship between POC and the maximum band ratio of remotesensing reflectance, MBR, where MBR is the highest value selected from the three reflectance band ratios,  $R_{rs}(443)/R_{rs}(555)$ ,  $R_{rs}(490)/R_{rs}(555)$ , and  $R_{rs}(510)/R_{rs}(555)$ . The blue, green, and orange lines depict the best-fit regression functions which represent the particle-composition classspecific algorithms for estimating POC from MBR for organic-dominated (Eq. (9a)), mixed (Eq. (9b)), and mineraldominated (Eq. (9c)) classes of suspended particulate matter, respectively. The data points depicted as blue open circles, green cross-marks, and orange triangles represent organic-dominated, mixed, mineral-dominated classes of suspended particulate matter, respectively. For comparison, the best-fit regression function for all data irrespective of particulate composition parameter, POC/SPM, is shown in black line. The corresponding equation is:

POC =  $10^{(2.32893-1.42557 \log(\text{MBR})+0.66318 [\log(\text{MBR})]^2-3.28291 [\log(\text{MBR})]^3)}$ . (b) The relationship between POC and remote-sensing reflectance band ratio,  $R_{rs}(443)/R_{rs}(555)$ . The data points representing measurements are compared with current standard global POC algorithm (black line) used by NASA OBPG. The equation of the standard algorithm is: POC =  $203.2 [R_{rs}(443)/R_{rs}(555)]^{-1.034}$  (Stramski et al., 2008). Only data for near-surface samples (N = 98) used in the development of  $R_{rs}$ -based algorithms are presented in this figure.

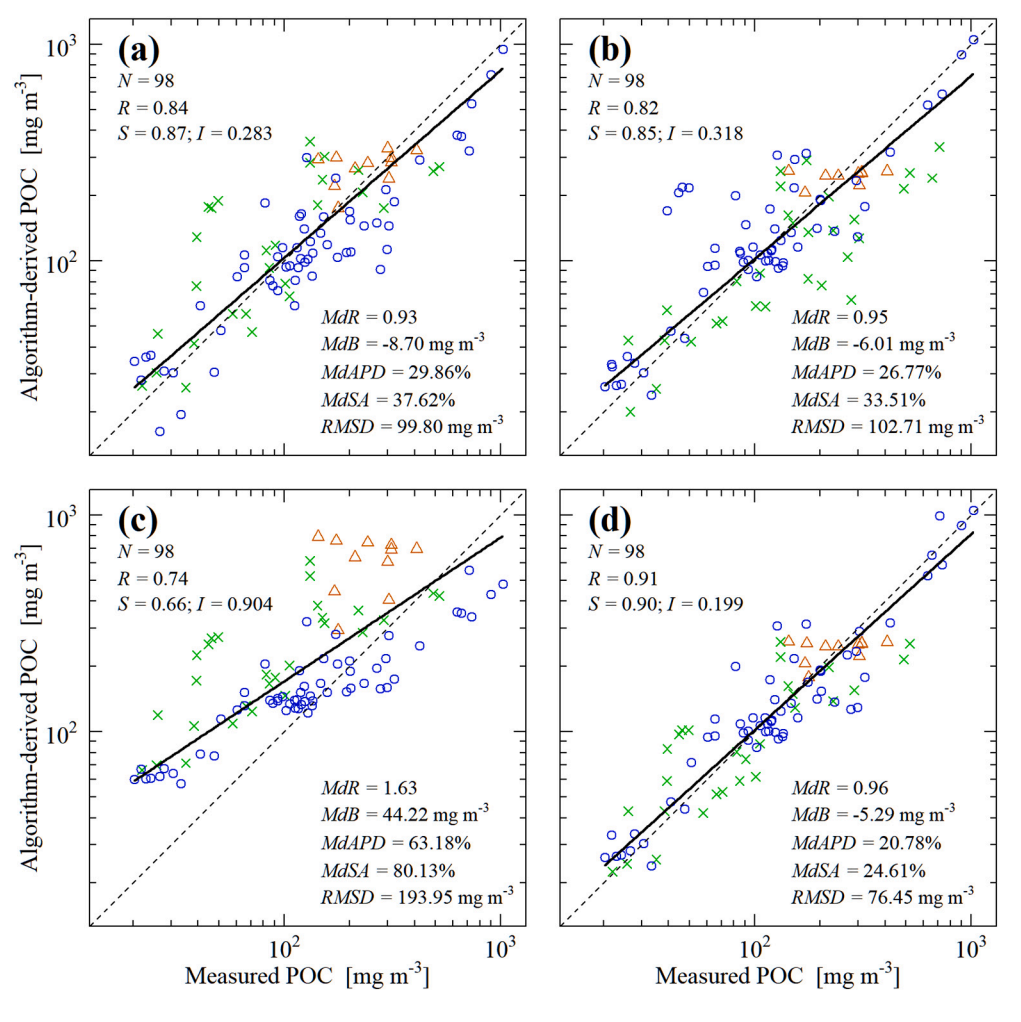


Fig. 14. Scatter plots comparing the algorithm-derived POC with measured POC for different variants of Rrs-based algorithms: (a) Method-1 particle compositionspecific algorithm utilizing Eq. (6a), (6b), (7a), (7b), and (8) for calculating POC, (b) Method-2 particle composition-specific algorithm utilizing Eq. (8) for POC/SPM-based classification and Eq. (9a), (9b), (9c) for calculating POC from class-specific formulas, (c) standard global POC algorithm (black line Fig. 13b), and (d) similar to (b) but POC/SPM-based classification was made using the measured values of POC/SPM instead of Eq. (8). For illustrative purposes, data points depicted as blue open circles, green cross-marks, and orange triangles represent the organic-dominated, mixed, and mineral-dominated classes of suspended particulate matter, respectively. The logtransformed data were used to calculate the correlation coefficient R and model-II linear regression fit (black solid line). The 1:1 line (dashed line) and several statistical parameters are also shown.

standard global POC algorithm used by NASA Ocean Biology Processing Group (OBPG) to generate the satellite-derived POC product from the reflectance band ratio  $R_{rs}(443)/R_{rs}(555)$  which was available on Sea-WiFS (Stramski et al., 2008; NASA Ocean Color Web https://oceancolor. gsfc.nasa.gov/atbd/poc/). Similar global algorithms based on the blueto-green reflectance band ratio are used by NASA OBPG for other satellite sensors. By design such global algorithms are intended primarily for use in open-ocean pelagic environments where surface waters are typically dominated by phytoplankton and co-varying organic matter (Stramski et al., 2008, 2022). Nevertheless, these algorithms are routinely applied to generate the global POC product indiscriminately across various water bodies encompassing large variation in particulate composition. Fig. 13b shows that the standard algorithm does not adequately represent the variability in the relationship between POC and reflectance observed in our field dataset that covers a wide dynamic range of particulate concentration and composition.

By comparing the algorithm-derived with measured POC, Fig. 14 illustrates the evaluation of particle composition-specific algorithms for estimating POC from  $R_{rs}(\lambda)$  using our algorithm development dataset. The comparison of the Method-1 algorithm (Fig. 14a) and the Method-2 algorithm (Fig. 14b) indicates similar performance with the MdR, MdR, MdAPD, and MdSA statistical parameters marginally better for the Method-2 algorithm and other statistics (R, S, I, RMSD) marginally better for the Method-1 algorithm. Importantly, the results in Fig. 14a,b demonstrate a superiority of composition-specific algorithms formulated with both Method-1 and Method-2 over the standard global POC algorithm (Fig. 14c). For example, while the RMSD and MdAPD values for the standard global algorithm are about 194 mg m<sup>-3</sup> and 63.2%

respectively (Fig. 14c), these statistics decrease about two-fold for the Method-1 (Fig. 14a) and Method-2 (Fig. 14b) algorithms. In addition, the standard global algorithm tends to produce significant positive bias across a broad range of POC with an aggregate measure of bias MdR =1.63. In contrast, the Method-1 and Method-2 algorithms do not produce significant biasing effects. This comparison, while demonstrating the known limitations of standard global algorithms for indiscriminate applications across diverse water bodies, supports the potential for improved performance of particle composition-specific algorithms. In addition, we note that the regression function fitted to all data regardless of POC/SPM (Fig. 13a, solid black line) also yields inferior statistics compared to the particle composition-specific algorithms. For example, the analysis of POC derived from this indiscriminate best-fit function vs. measured POC yielded RMSD of 132 mg m<sup>-3</sup>, S = 0.8 and I = 0.41, where the latter two parameters are indicative of significant positive and negative biases within the ranges of low and high POC, respectively.

Fig. 14d is provided for comparison with the Method-2 algorithm in Fig. 14b. The results in Fig. 14d were obtained with the compositional class assignment of  $R_{\rm rs}(\lambda)$  input to the class-specific formulas, i.e., the MBR input to Eqs. (9a), (9b), (9c) is based on measured POC/SPM rather than the algorithm-derived POC/SPM from Eq. (8). Thus, in contrast to the operational Method-2 algorithm shown in Fig. 14b which is subject to some misclassifications associated with the use of POC/SPM algorithm, the results in Fig. 14d are free of misclassification errors. Thus, the statistics in Fig. 14d are better than in Fig. 14b.

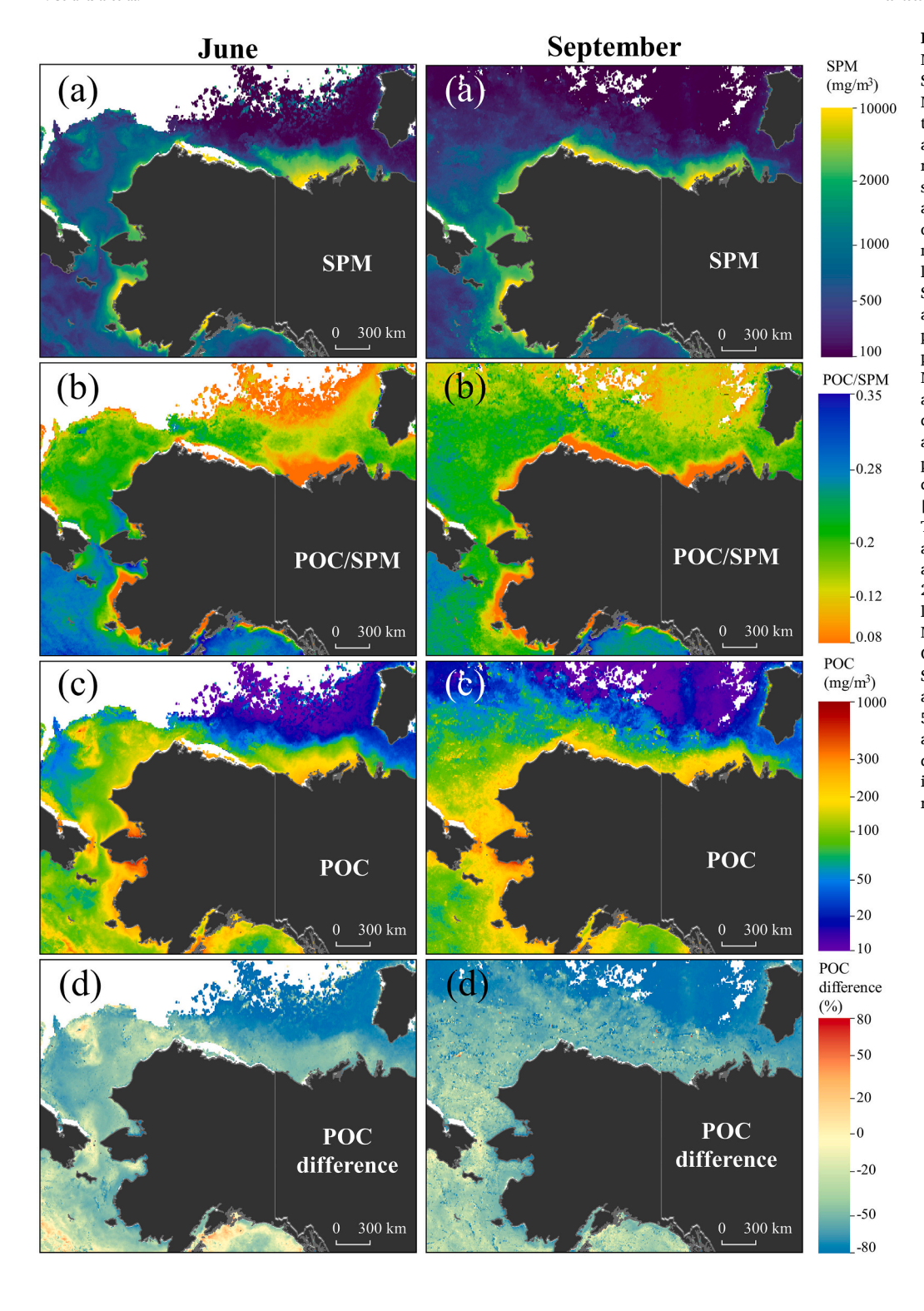


Fig. 15. (a) SPM derived from the MODIS-specific algorithm (Eqs. S1a, S1b and Table S1 in Supplementary Material). (b) POC/SPM derived from the MODIS-specific algorithm (Eq. S2 and Table S3 in Supplementary Material). (c) POC derived from the MODISspecific algorithm that uses Method-1 algorithm approach to account for the composition of particulate suspended matter. Specifically, POC was calculated as a product of algorithm-derived SPM shown in panel (a) and the algorithm-derived POC/SPM shown in panel (b). (d) Relative difference in percent between POC derived from the Method-1 particle composition-specific algorithm shown in panel (c) and POC derived from the standard global POC algorithm used by NASA OBPG for processing MODIS-Aqua imagery. This difference was calculated as 100  $\times$  $[POC_{method-1} - POC_{standard}]/POC_{standard}.$ These results represent the 10-year average data for the months of June and September over the period 2012-2021 obtained from daily satellite ocean color observations with MODIS-Aqua of the Beaufort Sea, the Chukchi Sea, and the northern Bering Sea (the latitude and longitude boundaries of the illustrated region are 57°-75° N; 125°-180° W). The white areas indicate the lack of valid satellite data, for example associated with sea ice cover in the northern part of the region.

## 3.4. Demonstration of application to satellite observations

Fig. 15 demonstrates the operational applicability of  $R_{\rm rs}$ -based algorithms for estimating SPM (Fig. 15a), POC/SPM (Fig. 15b), as well as POC using the Method-1 particle composition-specific algorithm (Fig. 15c) from satellite observations in the Arctic region encompassing the Beaufort Sea, the Chukchi Sea, and the northern portion of the Bering Sea. The results represent the 10-year average data for the months of June and September obtained from daily satellite observations with MODIS-Aqua over the period 2012–2021. These maps reveal

several salient features in the decadal averages of monthly characteristics of particulate assemblages in this Arctic region. For example, the elevated SPM observed around the coast of Alaska (Fig. 15a) is generally associated with relatively low POC/SPM indicative of significant or dominant contribution of mineral particles to SPM (Fig. 15b). The feature of elevated SPM and low POC/SPM produced by discharge of Mackenzie River has larger northward extent in the spring-to-summer transition period (June) than the summer-to-autumn transition period (September).

The northern part of the investigated region located south of the sea

ice cover includes surface waters with the lowest SPM (often <200 mg  $m^{-3}$ ; Fig. 15a) and lowest POC (<20 mg  $m^{-3}$ ; Fig. 15c). Interestingly, the POC/SPM retrievals indicate that these very clear waters can have low POC/SPM and thus be dominated by mineral particles (Fig. 15b). It is conceivable that this feature, which is especially well-pronounced in the June image of POC/SPM, may be related to release of particles from retreating sea ice. However, it must be noted that when SPM and POC are very low the retrievals of POC/SPM are susceptible to potential increase in relative error. It is also notable that whereas the POC/SPM maps reveal essentially no presence, or only minor presence, of distinct areas with clear dominance of organic particles (POC/SPM > 0.28) in the Chukchi and Beaufort Seas, large portions of this region have intermediate values of POC/SPM characteristic of mixed particulate assemblages (Fig. 15b). This lack of distinct areas with high POC/SPM may be largely related to the decadal scale of averaging the satellite observations. The POC maps derived from the particle composition-specific algorithm show generally elevated levels of POC in coastal waters (Fig. 15c). Another notable feature is the presence of extensive areas north and south of the Bering Strait which have higher POC in September than in June.

For comparison, Fig. 15d shows the relative difference in percent between POC derived from the Method-1 particle composition-specific algorithm and the current MODIS-specific standard global algorithm used by NASA OBPG. This difference was calculated as 100 imes[POC<sub>method-1</sub> - POC<sub>standard</sub>]/POC<sub>standard</sub>. The largest differences are generally observed in the northern portion of the region where POC retrieved from the particle-composition algorithm can be tens of percentage points lower relative to the standard POC product. In other areas including the waters adjacent to the Alaskan coast the differences are also significant. For the entire investigated region, the median difference in June is -37.4% and the 25th and 75th percentiles are -49.8% and -23.1%, respectively. In September these metrics of difference are -46.3%, -69.6%, and -33.1%, respectively. These results are most likely indicative of a tendency of POC overestimation by the standard global algorithm because it does not account for variations in the composition of suspended particulate matter. Such tendency to overestimate POC by the standard algorithm is consistent with the analysis of this algorithm with our algorithm development dataset as shown in Figs. 13b and 14c.

We have also generated the POC maps similar to those shown in Fig. 15c but using the Method-2 particle-composition class-specific algorithm. This result is shown in Fig. S5 (Supplementary Material). The spatial patterns of POC retrieved with the Method-1 and Method-2 algorithms are highly consistent. Given the differences in the design of the Method-1 and Method-2 algorithms, the POC estimates from these algorithms are expected to exhibit some differences which are also illustrated in Fig. S5. These results indicate, however, that the satellite-based retrievals of POC using the Method-1 and Method-2 algorithms are generally in good agreement to within  $\pm 10$  to 30%.

# 4. Summary and future perspectives

High complexity and variability in the composition of seawater constituents within the global ocean pose major challenges for the development of unified algorithm approaches for estimation of POC and other biogeochemically important constituents from optical observations across a continuum of diverse aquatic environments. To address these challenges, in this study we present an adaptive optical algorithm approach for estimating POC which accounts for variability in the composition of suspended particulate matter. We use the ratio of POC/SPM as a proxy for particulate composition to optically differentiate water bodies with varying proportions of organic and mineral particles. Using field data from the western Arctic seas that exhibit a broad range of water composition and optical properties, we developed empirical algorithms to estimate SPM and POC/SPM either from the particulate inherent optical properties (IOPs) of seawater (i.e., the spectral

absorption  $a_{\rm p}(\lambda)$  and backscattering  $b_{\rm bp}(\lambda)$  coefficients) or directly from the spectral remote-sensing reflectance of the ocean,  $R_{\rm rs}(\lambda)$ . The optical algorithms to retrieve POC/SPM enabled formulation of particle composition-specific algorithms for estimating POC either from particulate IOPs or from  $R_{\rm rs}(\lambda)$ . In each of these two algorithm categories we formulated the particle composition-specific algorithms to estimate POC from two methods. In the Method-1 algorithms POC is determined from the algorithm-derived SPM and POC/SPM. In the Method-2 algorithms POC is determined from particle composition class-specific formulas following POC/SPM-based classification of input optical data into one of the three particle-composition classes, i.e., organic-dominated, mineral-dominated, and mixed. In the category of  $R_{\rm rs}$ -based algorithms a suite of satellite sensor-specific algorithms was formulated which are applicable to observations with several past and current satellite ocean color missions.

The analysis of field data showed significant improvements in POC estimates from particle composition-specific algorithms in opticallycomplex Arctic waters compared with algorithms that do not account for variations in particulate composition, especially the current standard POC algorithm used for global satellite applications. We also demonstrated the example application of the  $R_{rs}$ -based algorithms to satellite ocean color observations in the Arctic region. Although our study uses data from the Arctic region, the underlying concept of adaptive algorithms based on optically-derivable characteristics of water constituents is not intended to be limited to specific regions but rather is expected to be more broadly applicable. Also, while the present study demonstrates the adaptive optical algorithms relying on the use of POC/SPM, the prospect of incorporation of additional water-constituent properties related, for example, to particle size distribution and CDOM has the potential to further improve the adaptive approach in terms of accounting for optical variability caused by water constituents across diverse environments.

Although the algorithms for estimating chlorophyll-a concentration (Chla) are outside the scope of this study, it is noteworthy that the particle composition-specific approach could be also useful to improve Chla retrievals from optical algorithms. This expectation is supported by our Arctic data of Chla plotted versus particulate IOPs in Fig. 16 which show qualitatively similar patterns to those for POC vs. IOPs in Fig. 6. Unsurprisingly, the data points in Fig. 16 are spread widely because chlorophyll-a is essentially found only in phytoplankton which coexist with many types of organic and inorganic particles suspended in water and multiple characteristics of phytoplankton and all other types of particles affect the relationships between Chla and particulate IOPs. However, Fig. 16 also shows that the observed data spread is largely associated with changes in particulate composition parameterized by POC/SPM. It is seen, for example, that samples dominated by organic particles with high values of POC/SPM exhibit relatively tight relationships, especially between Chla and  $a_p(\lambda)$  (Fig. 16a,b,c). As POC/ SPM decreases with decreasing contribution of organic particles, these relationships weaken.

Whereas the demonstrated capability to estimate POC/SPM from optical measurements provided a mechanistically-based framework for particle composition-specific algorithms to estimate POC, it is also noteworthy that POC/SPM can itself be a useful product for biogeochemical studies, for example, when investigating the role of mineral particles as ballast that enhances the export flux of POC from the surface layer to deep ocean, stimulation of primary productivity by aeolian input of iron-rich dust, or organic matter incorporation into sediments (e.g., Armstrong et al., 2001; Le Moigne et al., 2014; Schartau et al., 2019; Van der Jagt et al., 2018). In addition, the  $R_{\rm rs}$ -derived POC/SPM can provide a useful quality flag for current standard global products of POC and Chla derived from satellite ocean color missions, especially in waters dominated by mineral particles (i.e., low POC/SPM) where these standard products can be subject to gross error.

In closing, this study demonstrates that differentiation of water bodies based on particulate composition proxy of POC/SPM provides a

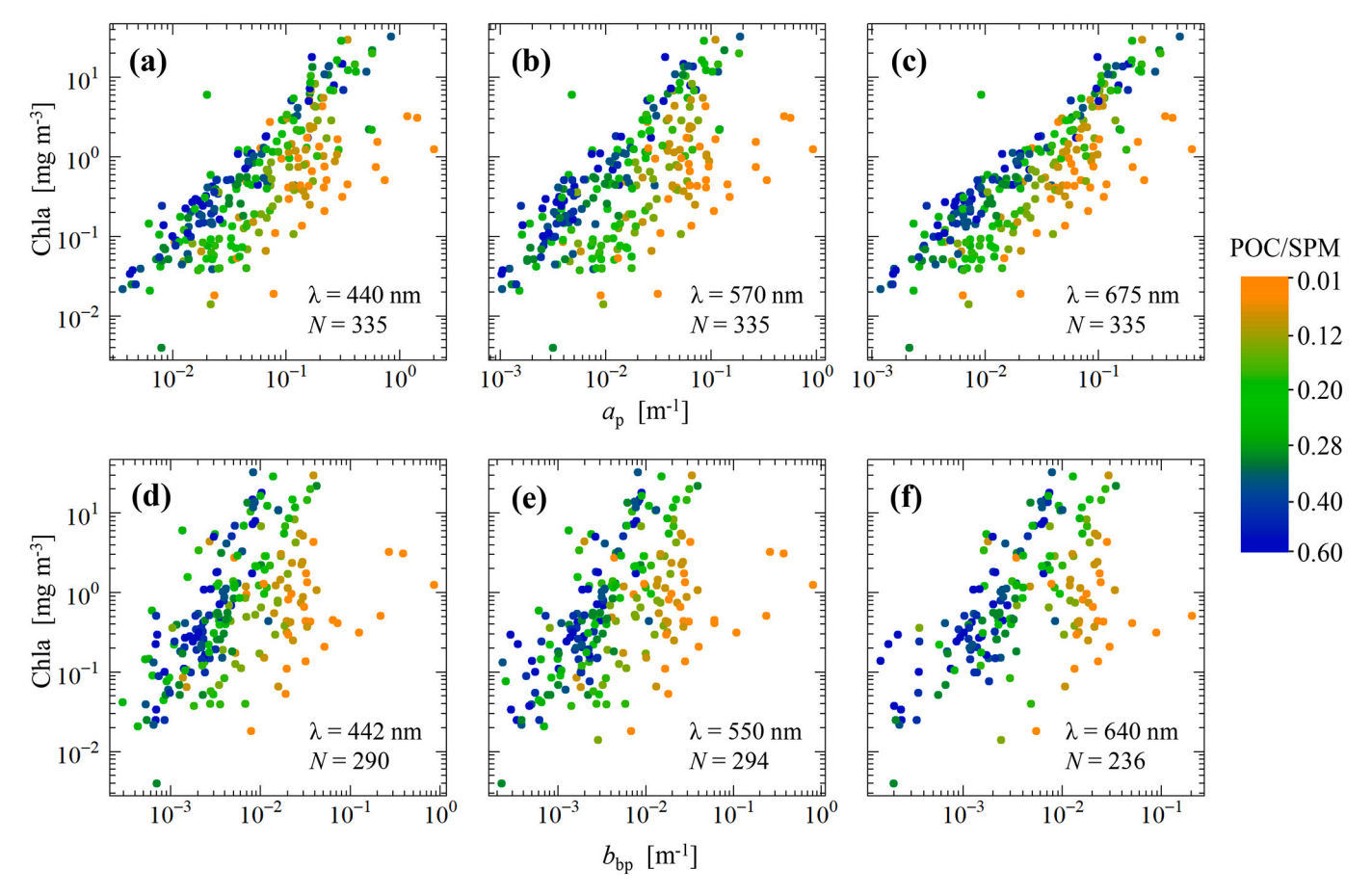


Fig. 16. As Fig. 6 but for the relationships between the concentration of chlorophyll-a, Chla, and the IOPs of suspended particles.

promising adaptive framework for optical algorithms with improved performance along the continuum of water bodies exhibiting large variability in particulate composition and optical properties. This supports a need for further evaluation of presented algorithms with independent field and satellite data from various regions to assess the performance and uncertainties under different application and environmental scenarios as well as explore further refinements and advancements in the adaptive algorithm approach that accounts for variability in cause-and-effect relationships between water-constituent properties and optical properties.

## Credit author statement

Conceptualization: DS, SC, RAR. Methodology: DS, SC, RAR. Data curation: RAR, DS, SC. Formal analysis: SC. Investigation: DS, SC, RAR. Writing - original draft: DS.

Writing - review & editing: DS, SC, RAR.

## **Declaration of Competing Interest**

Dariusz Stramski reports financial support was provided by NASA and NRL. Sorin Constantin reports financial support was provided by Fulbright Visiting Scholar Program and Romanian Ministry of Education and Research. Rick A. Reynolds reports financial support was provided by NASA and NSF.

## Data availability

Data will be made available on request.

# Acknowledgments

This work was supported by the U.S. National Aeronautics and Space Administration (NASA) [Grant 80NSSC18K0956], National Science Foundation (NSF) [Grant OPP-1822021], and Naval Research Laboratory (NRL) [Award N00173-22-2-C608]. Part of data analysis was made during a visit of S. Constantin to the Scripps Institution of Oceanography with support of Fulbright Visiting Scholar Program [Grant 675, September 2018]. His work was also supported by a grant of the Romanian Ministry of Education and Research, CNCS - UEFISCDI, project number PN-III-P1-1.1-PD-2019-0894 within PNCDI III. Field data used in this study were collected on four cruises in which the members of our lab at Scripps Institution of Oceanography participated with previous support from NASA. The ICESCAPE project was funded by NASA. The MALINA project was co-funded by the French Agence Nationale de la Recherche, L'Institut National des Sciences de l'Univers-Centre National de la Recherche Scientifique, Centre National d'Etudes Spatiales, the European Space Agency, the European Commission (Marie Skłodowska-Curie Actions), and the Canadian ArcticNet program. The ArCS project was funded by the Japanese Ministry of Education, Culture, Sports, Science and Technology. We thank K. Arrigo, M. Babin, S. Bélanger, D. Doxaran, J. Ehn, A. Fujiwara, T. Hirawake, S. Hooker, L. Li, A. Matsuoka, B. G. Mitchell, S. Nishino, J. Ras, S. Watanabe, and G. Zheng for assistance in the field and/or sharing of data. We also thank all scientists and crew on the cruises for additional support in fieldwork. Some radiometric data were obtained from the NASA Sea-WiFS Bio-Optical Archive and Storage System (SeaBASS; https://seaba

ss.gsfc.nasa.gov/). Special thanks go to the NASA Ocean Biology Processing Group for the production and distribution of the MODIS-Aqua remote-sensing reflectance data used in this study (2018 Reprocessing, NASA OB.DAAC, Greenbelt, MD, USA; https://doi.org/10.5067/AQUA/MODIS/L3M/RRS/2018, accessed on 09/02/2021). POC analysis of seawater samples was done at the Marine Science Institute, University of California Santa Barbara. We thank Kelsey Bisson and two anonymous reviewers for valuable comments on the manuscript.

## Appendix A. Supplementary Material

Supplementary material to this article can be found online at htt ps://doi.org/10.1016/j.rse.2022.113360.

#### References

- Aas, E., 1996. Refractive index of phytoplankton derived from its metabolite composition. J. Plankton Res. 18, 2223–2249. https://doi.org/10.1093/plankt/ 18.12.2223
- Allison, D.B., Stramski, D., Mitchell, B.G., 2010. Empirical ocean color algorithms for estimating particulate organic carbon in the Southern Ocean. J. Geophys. Res. 115, C10044. https://doi.org/10.1029/2009jc006040.
- Altman, D.G., Bland, J.M., 1983. Measurement in medicine: the analysis of method comparison studies. The Statistician 32, 307–317.
- Antoine, D., Hooker, S.B., Bélanger, S., Matsuoka, A., Babin, M., 2013. Apparent optical properties of the Canadian Beaufort Sea Part 1: Observational overview and water column relationships. Biogeosciences 10, 4493–4509. https://doi.org/10.5194/bg-10-4493-2013.
- Armstrong, R.A., Lee, C., Hedges, J.I., Honjo, S., Wakeham, Stuart G., S. G., 2001. A new, mechanistic model for organic carbon fluxes in the ocean based on the quantitative association of POC with ballast minerals. Deep Sea Res. Part II Top. Stud. Oceanogr. 49 (1–3), 219–236. https://doi.org/10.1016/S0967-0645(01)00101-1.
- Arrigo, K.R., 2015. Impacts of climate on ecosystems and chemistry of the Arctic Pacific environment (ICESCAPE). Deep-Sea Res. Part II Top. Stud. Oceanogr. 118, Part A, 1–6
- Babin, M., Morel, A., Fournier-Sicre, V., Fell, F., Stramski, D., 2003a. Light scattering properties of marine particles in coastal and open ocean waters as related to the particle mass concentration. Limnol. Oceanogr. 48, 843–859. https://doi.org/ 10.4319/lo.2003.48.2.0843.
- Babin, M., Stramski, D., Ferrari, G.M., Claustre, H., Bricaud, A., Obolensky, G., Hoepffner, N., 2003b. Variations in the light absorption coefficients of phytoplankton, non-algal particles, and dissolved organic matter in coastal waters around Europe. J. Geophys. Res. 108 (C7), 3211. https://doi.org/10.1029/ 2001 IC000882
- Balch, W.M., Bowler, B.C., Drapeau, D.T., Poulton, A.J., Holligan, P.M., 2010. Biominerals and the vertical flux of particulate organic carbon from the surface ocean. Geophys. Res. Lett. 37, L22605. https://doi.org/10.1029/2010GL044640.
- Behrenfeld, M.J., Hu, Y., Hostetler, C.A., Dall'olmo, G., Rodier, S.D., Hair, J.W., Trepte, C.R., 2013. Space-based lidar measurements of global ocean carbon stocks. Geophys. Res. Lett. 40, 4355–4360. https://doi.org/10.1002/grl.50816.
- Bellacicco, M., Vellucci, V., Scardi, M., Barbieux, M., Marullo, S., D'Ortenzio, F., 2019. Quantifying the impact of linear regression model in deriving bio-optical relationships: the implications on ocean carbon estimations. Sensors (Basel) 19 (13). https://doi.org/10.3390/s19133032.
- Betzer, P.R., Carder, K.L., Eggimann, D.W., 1974. Light scattering and suspended matter on a transect of the Atlantic Ocean at 11N. In: Gibbs, J.R. (Ed.), Suspended Solids in Water. Plenum Press, New York, pp. 295–314.
- Bisson, K.M., Boss, E., Werdell, P.J., Ibrahim, A., Frouin, R., Behrenfeld, M.J., 2021. Seasonal bias in global ocean color observations. Appl. Opt. 60, 6978–6988. https://doi.org/10.1364/A0.426137.
- Bland, J.M., Altman, D.G., 1983. Statistical method for assessing agreement between two methods of clinical measurement. Lancet 327 (8476), 307–310.
- Boss, E., Pegau, W.S., Lee, M., Twardowski, M.S., Shybanov, W., Korotaev, G., Baratange, F., 2004. The particulate backscattering ratio at LEO 15 and its use to study particles composition and distribution. J. Geophys. Res. 109, C01014. https://doi.org/10.1029/2002JC001514.
- Bowers, D.G., Binding, C.E., 2006. The optical properties of mineral suspended particles: a review and synthesis. Estuar. Coast. Shelf Sci. 67, 219–230. https://doi.org/ 10.1016/j.ecss.2005.11.010.
- Carder, K.L., Betzer, P.R., Eggimann, D.W., 1974. Physical, chemical and optical measures of suspended-particle concentrations: Their intercomparison and application to the west african shelf. In: Gibbs, R.J. (Ed.), Suspended Solids in Water. Plenum Press, New York, pp. 173–193.
- Cetinić, I., Perry, M.J., Briggs, N.T., Kallin, E., D'Asaro, E.A., Lee, C.M., 2012. Particulate organic carbon and inherent optical properties during 2008 North Atlantic bloom experiment. J. Geophys. Res. Oceans 117, C06028. https://doi.org/10.1029/2011JC007771.
- Claustre, H., Johnson, K.S., Takeshita, Y., 2020. Observing the global ocean with Biogeochemical-Argo. Annu. Rev. Mar. Sci. 12, 23–48. https://doi.org/10.1146/ annurev-marine-010419-010956.

- Doxaran, D., Froidefond, J.M., Castaing, P., 2002. A reflectance band ratio used to estimate suspended matter concentrations in sediment-dominated coastal waters. Int. J. Remote Sens. 23, 5079–5085. https://doi.org/10.1080/0143116021000009912.
- Doxaran, D., Ehn, J., Bélanger, S., Matsuoka, A., Hooker, S., Babin, M., 2012. Optical characterisation of suspended particles in the Mackenzie River plume (Canadian Arctic Ocean) and implications for ocean colour remote sensing. Biogeosciences 9, 3213–3229. https://doi.org/10.5194/bg-9-3213-2012.
- Eleveld, M.A., Ruescas, A.B., Hommersom, A., Moore, T.S., Peters, S.W.M., Brockmann, C., 2017. An optical classification tool for global lake waters. Remote Sens. 9, 420. https://doi.org/10.3390/rs9050420.
- Feely, R.A., Sullivan, L., Sackett, W.M., 1974. Light-scattering measurements and chemical analysis of suspended matter in the near-bottom nepheloid layer of the Gulf of Mexico. In: Gibbs, R.J. (Ed.), Suspended Solids in Water. Plenum Press, New York, pp. 281–293.
- Gardner, W.D., Richardson, M.J., Carlson, C.A., Hansell, D., Mishonov, A.V., 2003.
  Determining true particulate organic carbon: bottles, pumps and methodologies.
  Deep-Sea Res. II 50, 655–674. https://doi.org/10.1016/S0967-0645(02)00589-1.
- Gordon Jr., D.C., 1970. Some studies on the distribution and composition of particulate organic carbon in the North Atlantic Ocean. Deep-Sea Res. 17, 233–243. https://doi.org/10.1016/0011-7471(70)90017-3.
- Gordon, H., Morel, A., 1983. Remote assessment of ocean color for interpretation of satellite visible imagery: A review. In: Lecture Notes on Coastal and Estuarine Studies, Vol. 4. Springer Verlag, New York, pp. 1–114.
- Haëntjens, N., Boss, E., Talley, L.D., 2017. Revisiting ocean color algorithms for chlorophyll a and particulate organic carbon in the Southern Ocean using biogeochemical floats. J. Geophys. Res. Oceans 122, 6583–6593. https://doi.org/ 10.1002/2017JC012844.
- Han, B., Loisel, H., Vantrepotte, V., Meriaux, X., Bryere, P., Ouillon, S., Dessailly, D., Xing, Q., Zhu, J., 2016. Development of a semi-analytical algorithm for the retrieval of suspended particulate matter from remote sensing over clear to very turbid waters. Remote Sens. 8, 211. https://doi.org/10.3390/rs8030211.
- Hu, C., Chen, Z., Clayton, T., Swarzenski, P., Brock, J., Muller-Karger, F., 2004. Assessment of estuarine water-quality indicators using MODIS medium-resolution bands: initial results from Tampa Bay. FL. Remote Sens. Environ. 93, 423–441. https://doi.org/10.1016/j.rse.2004.08.007.
- Intergovernmental Oceanographic Commission, 1994. Protocols for the Joint Global Ocean Flux Study (JGOFS) core measurements. Intergovernmental Oceanographic Commission, Scientific Committee on Oceanic Research, Manuals and Guides no. 29. In: UNESCO-IOC, Paris, pp. 1–170.
- IOCCG Protocol Series, 2019. Protocols for satellite ocean colour data validation: in situ optical radiometry. In: Zibordi, G., Voss, K.J., Johnson, B.C., Mueller, J.L. (Eds.), IOCCG Ocean Optics and Biogeochemistry Protocols for Satellite Ocean Colour Sensor Validation, Volume 3.0. IOCCG, Dartmouth, NS, Canada. https://doi.org/10.25607/OBP-691.
- IOCCG Protocol Series, 2021. Particulate organic matter sampling and measurement protocols: consensus towards future ocean color missions. In: Chaves, J.E., Cetinić, I., Dall'olmo, G., Estapa, M., Gardner, W., Goñi, M., Graff, J.R., Hernes, P., Lam, P.J., Liu, Z., Lomas, M.W., Mannino, M., Novak, M.G., Turnewitsch, R., Werdell, P.J., Westberry, T.K. (Eds.), IOCCG Ocean Optics and Biogeochemistry Protocols for Satellite Ocean Colour Sensor Validation, Volume 6.0. IOCCG, Dartmouth, NS, Canada. https://doi.org/10.25607/OBP-1646.
- Jerlov, N.G., 1976. Marine Optics. Elsevier, Amsterdam.
- Johnson, K.S., Plant, J.N., Coletti, L.J., Jannasch, H.W., Sakamoto, C.M., Riser, S.C., Swift, D.D., Williams, N.L., Boss, E., Haëntjens, N., Talley, L.D., Sarmiento, J.L., 2017. Biogeochemical sensor performance in the SOCCOM profiling float array. J. Geophys. Res. Oceans 122, 6416–6436. https://doi.org/10.1002/2017JC012838.
- Jonasz, M., Fournier, G.R., 2007. Light Scattering by Particles in Water. Theoretical and Experimental Foundations. Academic Press, Amsterdam.
- Jorge, D.S.F., Loisel, H., Jamet, C., Dessailly, D., Demaria, J., Bricaud, A., Maritorena, S., Zhang, X., Antoine, D., Kutser, T., Bélanger, S., Brando, V.O., Werdell, J., Kwiatkowska, E., Mangin, A., Fanton d'Andon, O., 2021. A three-step semi analytical algorithm (3SAA) for estimating inherent optical properties over oceanic, coastal, and inland waters from remote sensing reflectance. Remote Sens. Environ. 263, 112537 https://doi.org/10.1016/j.rse.2021.112537.
- Kermack, K.A., Haldane, J.B.S., 1950. Organic correlation and allometry. Biometrika 37, 30–41.
- Koestner, D., Stramski, D., Reynolds, R.A., 2022. A multivariable empirical algorithm for estimating particulate organic carbon concentration in marine environments from optical backscattering and chlorophyll-a measurements. Front. Mar. Sci. 9, 941950 https://doi.org/10.3389/fmars.2022.941950.
- Kostakis, I., Twardowski, M., Roesler, C., Röttgers, R., Stramski, D., McKee, D., Tonizzo, A., Drapeau, S., 2021. Hyperspectral optical absorption closure experiment in complex coastal waters. Limnol. Oceanogr. Methods 19, 589–625. https://doi. org/10.1002/lom3.10447.
- Lahet, F., Ouillon, S., Forget, P., 2001. Colour classification of coastal waters of the Ebro river plume from spectral reflectances. Int. J. Remote Sens. 22 (9), 1639–1664. https://doi.org/10.1080/01431160118523.
- Le Moigne, F.A.C., Pabortsava, K., Marcinko, C.L.J., Martin, P., Sanders, R.J., 2014. Where is mineral ballast important for surface export of particulate organic carbon in the ocean? Geophys. Res. Lett. 41, 8460–8468. https://doi.org/10.1002/2014GL061678.
- Le, C., Li, Y., Zha, Y., Sun, D., Huang, C., Zhang, H., 2011. Remote estimation of chlorophyll a in optically complex waters based on optical classification. Remote Sens. Environ. 115, 725–737. https://doi.org/10.1016/j.rse.2010. 10.014.

- Lee, Z.P., Carder, K.L., Arnone, R.A., 2002. Deriving inherent optical properties from water color: a multiband quasi-analytical algorithm for optically deep waters. Appl. Opt. 41, 5755–5772. https://doi.org/10.1364/AO.41.005755.
- Legendre, L., Michaud, J., 1999. Chlorophyll a to estimate the particulate organic carbon available as food to large zooplankton in the euphotic zone of oceans. J. Plankton Res. 21, 2067–2083. https://doi.org/10.1093/plankt/21.11.2067.
- Lewis, K.M., Mitchell, B.G., van Dijken, G.L., Arrigo, K.R., 2016. Regional chlorophyll a algorithms in the Arctic Ocean and their effect on satellite-derived primary production estimates. Deep-Sea Res. Part II 130, 14–27. https://doi.org/10.1016/j. dsr2.2016.04.020.
- Li, L., Stramski, D., Reynolds, R.A., 2016. Effects of inelastic radiative processes on the determination of water-leaving spectral radiance from extrapolation of underwater near-surface measurements. Appl. Opt. 55, 7050–7067. https://doi.org/10.1364/ A0.55.007050.
- Loisel, H., Mériaux, X., Berthon, J.-F., Poteau, A., 2007. Investigation of the optical backscattering to scattering ratio of marine particles in relation to their biogeochemical composition in the eastern English Channel and southern North Sea. Limnol. Oceanogr. 52 (2), 739–752. https://doi.org/10.4319/lo.2007.52.2.0739.
- Loisel, H., Stramski, D., 2000. Estimation of the inherent optical properties of natural waters from the irradiance attenuation coefficient and reflectance in the presence of Raman scattering. Appl. Opt. 39, 3001–3011. https://doi.org/10.1364/
- Loisel, H., Stramski, D., Dessailly, D., Jamet, C., Li, L., Reynolds, R.A., 2018. An inverse model for estimating the optical absorption and backscattering coefficients of seawater from remote-sensing reflectance over a broad range of oceanic and coastal marine environments. J. Geophys. Res. Oceans 123, 2141–2171. https://doi.org/ 10.1002/2017.IC013632
- Lu, X., Hu, Y., Yang, Y., Neumann, T., Omar, A., Baize, R., Vaughan, M., Rodier, S., Getzewich, B., Lucker, P., Trepte, C., Hostetler, C., Winker, D., 2021. New Ocean subsurface optical properties from space lidars: CALIOP/CALIPSO and ATLAS/ ICESat-2. Earth Space Sci. 8, e2021EA001839. https://doi.org/10.1029/ 2021EA001839.
- Lubac, B., Loisel, H., 2007. Variability and classification of remote sensing reflectance spectra in the eastern English Channel and southern North Sea. Remote Sens. Environ. 110, 45–58. https://doi.org/10.1016/j.rse.2007.02.012.
- Massicotte, P., Amon, R.M.W., Antoine, D., Archambault, P., Balzano, S., Bélanger, S., Benner, R., Boeuf, D., Bricaud, A., Bruyant, F., Chaillou, G., Chami, M., Charrière, B., Chen, J., Claustre, H., Coupel, P., Delsaut, N., Doxaran, D., Ehn, J., Fichot, C., Forget, M.-H., Fu, P., Gagnon, J., Garcia, N., Gasser, B., Ghiglione, J.-F., Gorsky, G., Gosselin, M., Gourvil, P., Gratton, Y., Guillot, P., Heipieper, H.J., Heussner, S., Hooker, S.B., Huot, Y., Jeanthon, C., Jeffrey, W., Joux, F., Kawamura, K., Lansard, B., Leymarie, E., Link, H., Lovejoy, C., Marec, C., Marie, D., Martin, J., Martín, J., Massé, G., Matsuoka, A., McKague, V., Mignot, A., Miller, W.L., Miquel, J.-C., Mucci, A., Ono, K., Ortega-Retuerta, E., Panagiotopoulos, C., Papakyriakou, T., Picheral, M., Prieur, L., Raimbault, P., Ras, J., Reynolds, R.A., Rochon, A., Rontani, J.-F., Schmechtig, C., Schmidt, S., Sempéré, R., Shen, Y., Song, G., Stramski, D., Tachibana, E., Thirouard, A., Tolosa, I., Tremblay, J.-É., Vaïtilingom, M., Vaulot, D., Vaultier, F., Volkman, J.K., Xie, H., Zheng, G., Babin, M., 2021. The MALINA oceanographic expedition: how do changes in ice cover, permafrost and UV radiation impact biodiversity and biogeochemical fluxes in the Arctic Ocean? Earth Syst. Sci. Data 13, 1561–1592. https://doi.org/10.5194/essd-
- Matthews, M.W., 2011. A current review of empirical procedures of remote sensing in inland and near-coastal transitional waters. Int. J. Remote Sens. 32, 6855–6899. https://doi.org/10.1080/01431161.2010.512947.
- Mélin, F., Vantrepotte, V., Clerici, M., D'Alimonte, D., Zibordi, G., Berthon, J., Canuti, E., 2011. Multi-sensor satellite time series of optical properties and chlorophyll-a concentration in the Adriatic Sea. Prog. Oceanogr. 91, 229–244. https://doi.org/ 10.1016/j.pocean.2010.12.001.
- Mélin, F., Vantrepotte, V., 2015. How optically diverse is the coastal ocean? Remote Sens Environ 160, 235–251. https://doi.org/10.1016/j.rse.2015.01.023
- Sens. Environ. 160, 235–251. https://doi.org/10.1016/j.rse.2015.01.023.

  Miller, R.L., McKee, B.A., 2004. Using MODIS 250 m imagery to map concentrations of total suspended matter in coastal waters. Remote Sens. Environ. 93, 259–266. https://doi.org/10.1016/j.rse.2004.07.012.
- Mobley, C.D., 1994. Light and Water. Radiative Transfer in Natural Waters. Academic Press, San Diego, California.
- Moore, T.S., Campbell, J.W., Feng, H., 2001. A fuzzy logic classification scheme for selecting and blending satellite ocean color algorithms. IEEE Trans. Geosci. Remote Sens. 39 (8), 1764–1776. https://doi.org/10.1109/36.942555.
- Moore, T.S., Campbell, J.W., Dowell, M.D., 2009. A class-based approach to characterizing and mapping the uncertainty of the MODIS ocean chlorophyll product. Remote Sens. Environ. 113, 2424–2430. https://doi.org/10.1016/j. rsc.2009.07.016.
- Moore, T.S., Dowell, M.D., Bradt, S., Ruiz Verdu, A.H., 2014. An optical water type framework for selecting and blending retrievals from bio-optical algorithms in lakes and coastal waters. Remote Sens. Environ. 143, 97–111. https://doi.org/10.1016/j. rse.2013.11.021.
- Morel, A., 1973. Diffusion de la lumière par les eaux de mer; résultats expérimentaux et approche théorique. [The scattering of light by sea water: Experimental results and theoretical approach]. In: Optics of the Sea, Interface, and In-water Transmission and Imaging, pp. 3.1.1–3.1.76. NATO AGARD Lect. Ser. 61.
- Morel, A., Prieur, L., 1977. Analysis of variations in ocean color. Limnol. Oceanogr. 22 (4), 709–722. https://doi.org/10.4319/lo.1977.22.4.0709.
- Morley, S.K., 2016. Alternatives to accuracy and bias metrics based on percentage errors for radiation belt modeling applications. In: Tech. Rep. LA-UR-16-24592. Los Alamos National Laboratory, Los Alamos, New Mexico. https://doi.org/10.2172/1260362.

- Morley, S.K., Brito, T.V., Welling, D.T., 2018. Measures of model performance based on the log accuracy ratio. Space Weather 16, 69–88. https://doi.org/10.1002/ 2017SW001669.
- Mueller, J.L., 2003. Overview of measurement and data analysis methods. In: Mueller, J. L., Fargion, G.S., McClain, C.R. (Eds.), Ocean Optics Protocols for Satellite Ocean Color Sensor Validation, Revision 4, Volume III: Radiometric Measurements and Data Analysis Protocols, NASA Tech. Memo. 2003–211621/Revision 4 Vol. III. NASA Goddard Space Flight Center, Greenbelt, Maryland, pp. 1–20.
- Nechad, B., Ruddick, K.G., Park, Y., 2010. Calibration and validation of a generic multisensor algorithm for mapping of total suspended matter in turbid waters. Remote Sens. Environ. 114, 854–866. https://doi.org/10.1016/j.rse.2009.11.022.
- Neil, C., Spyrakos, E., Hunter, P., Tyler, A., 2019. A global approach for chlorophyll-a retrieval across optically complex inland waters based on optical water types. Remote Sens. Environ. 229, 159–178. https://doi.org/10.1016/j. rse.2019.04.027.
- Nelson, N.B., Siegel, D.A., 2013. The global distribution and dynamics of chromophoric dissolved organic matter. Annu. Rev. Mar. Sci. 5, 447–476. https://doi.org/10.1146/ annurey-marine-120710-100751.
- Neukermans, G., Loisel, H., Mériaux, X., Astoreca, R., McKee, D., 2012. In situ variability of mass-specific beam attenuation and backscattering of marine particles with respect to particle size, density, and composition. Limnol. Oceanogr. 57 (1), 124–144. https://doi.org/10.4319/lo.2012.57.1.0124.
- Neukermans, G., Reynolds, R.A., Stramski, D., 2016. Optical classification and characterization of marine particle assemblages within the western Arctic Ocean. Limnol. Oceanogr. 61, 1472–1494. https://doi.org/10.1002/lno.10316.
- Novak, M.G., Cetinič, I., Chaves, J.E., Mannino, A., 2018. The adsorption of dissolved organic carbon onto glass fiber filters and its effect on the measurement of particulate organic carbon: a laboratory and modeling exercise. Limnol. Oceanogr. Methods 16, 356–366. https://doi.org/10.1002/lom3.10248.
- Novoa, S., Doxaran, D., Ody, A., Vanhellemont, Q., Lafon, V., Lubac, B., Gernez, P., 2017. Atmospheric corrections and multi-conditional algorithm for multi-sensor remote sensing of suspended particulate matter in low-to-high turbidity levels coastal waters. Remote Sens. 9, 61. https://doi.org/10.3390/rs9010061.
- Odermatt, D., Gitelson, A., Brando, V.E., Schaepman, M., 2012. Review of constituent retrieval in optically deep and complex waters from satellite imagery. Remote Sens. Environ. 118, 116–126. https://doi.org/10.1016/j.rse.2011.11.013.
- Ondrusek, M., Stengel, E., Kinkade, C.S., Vogel, R.L., Keegstra, P., Hunter, C., Kim, C., 2012. The development of a new optical total suspended matter algorithm for the Chesapeake Bay. Remote Sens. Environ. 119, 243–254. https://doi.org/10.1016/j. rse.2011.12.018.
- O'Reilly, J.E., Maritorena, S., Mitchell, G., Siegel, D., Carder, K., Garver, S., Kahru, M., McClain, C.R., 1998. Ocean color chlorophyll algorithms for SeaWiFS. J. Geophys. Res. 103, 24937–24953. https://doi.org/10.1029/98JC02160.
- O'Reilly, J.E., Werdell, P.J., 2019. Chlorophyll algorithms for ocean color sensors OC4, OC5 & OC6. Remote Sens. Environ. 229, 32–47. https://doi.org/10.1016/j.rse.2019.04.021.
- Ouillon, S., Douillet, P., Petrenko, A., Neveux, J., Dupouy, C., Froidefond, J.-M., Andréfouët, S., Muñoz-Caravaca, A., 2008. Optical algorithms at satellite wavelengths for total suspended matter in tropical coastal waters. Sensors 8, 4165–4185. https://doi.org/10.3390/s8074165.
- Parsons, T.R., Maita, Y., Lalli, C.M., 1984. A Manual of Chemical and Biological Methods for Seawater Analysis. Pergamon Press, Oxford, England.
- Preisendorfer, R.W., 1961. Application of radiative transfer to theory to light measurements in the sea. Union Géodés. Géophys. Int. Monogr. Ser. 10, 11–30.
- Ras, J., Uitz, J., Claustre, H., 2008. Spatial variability of phytoplankton pigment distributions in the subtropical South Pacific Ocean: comparison between in situ and modelled data. Biogeosciences 5, 353–369. https://doi.org/10.5194/bg-5-353-2008.
- Reinart, A., Herlevi, A., Arst, H., Sipelgas, L., 2003. Preliminary optical classification of lakes and coastal waters in Estonia and South Finland. J. Sea Res. 49, 357–366. https://doi.org/10.1016/S1385-1101(03)00019-4.
- Reynolds, R.A., Stramski, D., 2019. Optical characterization of marine phytoplankton assemblages within surface waters of the western Arctic Ocean. Limnol. Oceanogr. 64, 2478–2496. https://doi.org/10.1002/lno.11199.
- Reynolds, R.A., Stramski, D., Neukermans, G., 2016. Optical backscattering of particles in Arctic seawater and relationships to particle mass concentration, size distribution, and bulk composition. Limnol. Oceanogr. 61, 1869–1890. https://doi.org/10.1002/ lno.10341.
- Ricker, W.E., 1973. Linear regressions in fishery research. J. Fish. Res. Board Can. 30, 409–434. https://doi.org/10.1139/f73-072.
- Riley, G.A., 1970. Particulate organic matter in sea water. Adv. Mar. Biol. 8, 1–118. https://doi.org/10.1016/80065-2881(08)60491-5.
- Roesler, C., Stramski, D., D'Sa, E.J., Röttgers, R., Reynolds, R.A., 2018. Spectrophotometric measurements of particulate absorption using filter pads. In: Neeley, A.R., Mannino, A. (Eds.), Ocean Optics & Biogeochemistry Protocols for Satellite Ocean Colour Sensor Validation. Volume 1: Inherent Optical Property Measurements and Protocols: Absorption Coefficient (vl.O), IOCCG Protocol Series. IOCCG, Dartmouth, Canada, pp. 50–73. https://doi.org/10.25607/OBP-119.
- Royston, P., 1995. Remark AS R94: a remark on algorithm AS181: the W-test for normality. J. R. Stat. Soc. 44 (4), 547–551.
- Runyan, H., Reynolds, R.A., Stramski, D., 2020. Evaluation of particle size distribution metrics to estimate the relative contributions of different size fractions based on measurements in Arctic waters. J. Geophys. Res. Oceans 125, e2020JC016218. https://doi.org/10.1029/2020JC016218.
- Schartau, M., Riethmüller, R., Flöser, G., van Beusekom, J.E.E., Krasemann, H., Hofmeister, R., Wirtz, K., 2019. On the separation between inorganic and organic fractions of suspended matter in a marine coastal environment. Prog. Oceanogr. 171, 231–250. https://doi.org/10.1016/j.pocean.2018.12.011.

- Seegers, B.N., Stumpf, R.P., Schaeffer, B.A., Loftin, K.A., Werdell, P.J., 2018.
  Performance metrics for the assessment of satellite data products: an ocean color case study. Opt. Express 26, 7404–7442. https://doi.org/10.1364/OE.26.007404.
- Shapiro, S.S., Wilk, M.B., 1965. An analysis of variance test for normality (complete samples). Biometrika 52 (3/4), 591–611. https://doi.org/10.1093/biomet/52.3-4.591.
- Shiozaki, T., Ijichi, M., Fujiwara, A., Makabe, A., Nishino, S., Yoshikawa, C., Harada, N., 2019. Factors regulating nitrification in the Arctic Ocean: potential impact of sea ice reduction and ocean acidification. Glob. Biogeochem. Cycles 33, 1085–1099. https://doi.org/10.1029/2018GB006068.
- Siswanto, E., Tang, J., Yamaguchi, H., Yuhwan, A., Ishizaka, J., Yoo, S., Sangwoo, K., Kiyomoto, Y., Yamada, K., Chiang, C., Kawamura, H., 2011. Empirical Ocean-color algorithms to retrieve chlorophyll-a, total suspended matter, and colored dissolved organic matter absorption coefficient in the yellow and East China seas. J. Oceanogr. 67, 627–650. https://doi.org/10.1007/s10872-011-0062-z.
- Snyder, W.A., Arnone, R.A., Davis, C.O., Goode, W., Gould, R.W., Ladner, S., Lamella, G., Rhea, W.J., Stavn, R., Sydor, M., Weidemann, A., 2008. Optical scattering and backscattering by organic and inorganic particulates in U.S. Coastal waters. Appl. Opt. 47, 666–677. https://doi.org/10.1364/AO.47.000666.
- Sokal, R.R., Rohlf, F.J., 1995. Biometry: The Principles and Practice of Statistics in Biological Research. In: 3rd edition. W. H. Freeman and Co., New York.
- Spyrakos, E., O'Donnell, R., Hunter, P.D., Miller, C., Scott, M., Simis, S.G.H., Neil, C., Barbosa, C.C.F., Binding, C.E., Bradt, S., Bresciani, M., Dall'Olmo, G., Giardino, C., Gitelson, A.A., Kutser, T., Li, L., Matsushita, B., Martinez-Vicente, V., Matthews, M. W., Ogashawara, I., Ruiz-Verd, A., Schalles, J.F., Tebbs, E., Zhang, Y., Tyler, A.N., 2018. Optical types of inland and coastal waters. Limnol. Oceanogr. 63, 846–870. https://doi.org/10.1002/ino.10674.
- Stavn, R.H., Richter, S.J., 2008. Biogeo-optics: particle optical properties and the partitioning of the spectral scattering coefficient of ocean waters. Appl. Opt. 47, 2660–2679. https://doi.org/10.1364/AO.47.002660.
- Stramski, D., Kiefer, D.A., 1991. Light scattering by microorganisms in the open ocean. Prog. Oceanogr. 28, 343–383. https://doi.org/10.1016/0079-6611(91)90032-H.
- Stramski, D., Reynolds, R.A., Kahru, M., Mitchell, B.G., 1999. Estimation of particulate organic carbon in the ocean from satellite remote sensing. Science 285, 239–242. https://doi.org/10.1126/science.285.5425.239.
- Stramski, D., Babin, M., Woźniak, S.B., 2007. Variations in the optical properties of terrigenous mineral-rich particulate matter suspended in seawater. Limnol. Oceanogr. 52, 2418–2433. https://doi.org/10.4319/lo.2007.52.6.2418.
- Stramski, D., Reynolds, R.A., Babin, M., Kaczmarek, S., Lewis, M.R., Röttgers, R., Sciandra, A., Stramska, M., Twardowski, M.S., Franz, B.A., Claustre, H., 2008. Relationships between the surface concentration of particulate organic carbon and optical properties in the eastern South Pacific and eastern Atlantic oceans. Biogeosciences 5, 171–201. https://doi.org/10.5194/bg-5-171-2008.
- Stramski, D., Reynolds, R.A., Kaczmarek, S., Uitz, J., Zheng, G., 2015. Correction of pathlength amplification in the filter-pad technique for measurements of particulate absorption coefficient in the visible spectral region. Appl. Opt. 54, 6763–6782. https://doi.org/10.1364/AO.54.006763.
- Stramski, D., Li, L., Reynolds, R.A., 2019. Model for separating the contributions of non-algal particles and colored dissolved organic matter to light absorption by seawater. Appl. Opt. 58, 3790–3806. https://doi.org/10.1364/AO.58.003790.
- Stramski, D., Joshi, I., Reynolds, R.A., 2022. Ocean color algorithms to estimate the concentration of particulate organic carbon in surface waters of the global ocean in support of a long-term data record from multiple satellite missions. Remote Sens. Environ. 269, 112776. https://doi.org/10.1016/j.rse.2021.112776.
- Tran, T.K., Duforèt-Gaurier, L., Vantrepotte, V., Jorge, D.S.F., Mériaux, X., Cauvin, A., Fanton d'Andon, O., Loisel, H., 2019. Deriving particulate organic carbon in coastal waters from remote sensing: inter-comparison exercise and development of a maximum band-ratio approach. Remote Sens. 11, 2849. https://doi.org/10.3390/
- Twardowski, M.S., Boss, E., MacDonald, J.B., Pegau, W.S., Barnard, A.H., Zaneveld, J.R. V., 2001. A model for estimating bulk refractive index from optical backscattering ratio and the implications for understanding particle composition in case I and case II waters. J. Geophys. Res. 106, 14129–14142. https://doi.org/10.1029/2000IC000404
- Twardowski, M.S., Claustre, H., Freeman, S.A., Stramski, D., Huot, Y., 2007. Optical backscattering properties of the "clearest" natural waters. Biogeosciences 4, 1041–1058. https://doi.org/10.5194/bg-4-1041-2007.
- Tyler, A.N., Hunter, P.D., Spyrakos, E., Groom, S., Constantinescu, A.M., Kitchen, J., 2016. Developments in earth observation for the assessment and monitoring of inland, transitional, coastal and shelf-sea waters. Sci. Total Environ. 572, 1307–1321. https://doi.org/10.1016/j.scitotenv.2016.01.020.
- Uitz, J., Stramski, D., Reynolds, R.A., Dubranna, J., 2015. Assessing phytoplankton community composition from hyperspectral measurements of phytoplankton

- absorption coefficient and remote-sensing reflectance in open-ocean environments. Remote Sens. Environ. 171, 58-74. https://doi.org/10.1016/j.rse.2015.09.027.
- Van der Jagt, H., Friese, C., Stuut, J.-B.W., Fischer, G., Iversen, M.H., 2018. The ballasting effect of saharan dust deposition on aggregate dynamics and carbon export: aggregation, settling, and scavenging potential of marine snow. Limnol. Oceanogr. 63, 1386–1394. https://doi.org/10.1002/lno.10779.
- Van der Linde, D.W., 1998. Protocol for the determination of total suspended matter in oceans and coastal zones. Joint Research Centre, Ispra, Italy. Technical Note I.98.182.
- Van Heukelem, L., Thomas, C.S., 2001. Computer-assisted high-performance liquid chromatography method development with applications to the isolation and analysis of phytoplankton pigments. J. Chromatogr. A 910, 31–49. https://doi.org/10.1016/ s0378-4347(00)00603-4
- Vantrepotte, V., Loisel, H., Dessailly, D., Mériaux, X., 2012. Optical classification of contrasted coastal waters. Remote Sens. Environ. 123, 306–323. https://doi.org/ 10.1016/j.rse.2012.03.004.
- Wei, J., Wang, M., Jiang, L., Yu, X., Mikelsons, K., Shen, F., 2021. Global estimation of suspended particulate matter from satellite ocean color imagery. J. Geophys. Res. Oceans 126, e2021JC017303. https://doi.org/10.1029/2021JC017303.
- Werdell, P.J., Franz, B.A., Bailey, S.W., Feldman, G.C., Boss, E., Brando, V.E., Dowell, M., Hirata, T., Lavender, S.J., Lee, Z.P., Loisel, H., Maritorena, S., Mélin, S., Moore, T.S., Smyth, T.J., Antoine, D., Devred, E., Hembise Fanton d'Andon, O., Mangin, A., 2013. Generalized ocean color inversion model for retrieving marine inherent optical properties. Appl. Opt. 52, 2019–2037. https://doi.org/10.1364/AO.52.002019.
- Werdell, J.P., McKinna, L.I.W., Boss, E., Ackleson, S.G., Craig, S.E., Gregg, W.W., Lee, Z., Maritorena, S., Roesler, C.S., Rousseaux, C.S., Stramski, D., Sullivan, J.M., Twardowski, M.S., Tzortziou, M., Zhang, X., 2018. An overview of approaches and challenges for retrieving marine inherent optical properties from ocean color remote sensing. Prog. Oceanogr. 160, 186–212. https://doi.org/10.1016/j.pocean.2018.01.001.
- Werdell, P.J., Behrenfeld, M.J., Bontempi, P.S., Boss, E., Cairns, B., Davis, G.T., Franz, B. A., Gliese, U.B., Gorman, E.T., Hasekamp, O., Knobelspiesse, K.D., Mannino, A., Martins, J.V., McClain, C.R., Meister, G., Remer, L., 2019. The Plankton, Aerosol, Cloud, ocean Ecosystem (PACE) mission: status, science, advances. Bull. Am. Meteorol. Soc. 100, 1775–1794. https://doi.org/10.1175/BAMS-D-18-0056.1.
  Woźniak, B., Dera, J., 2007. Light Absorption in Sea Water. Springer, New York.
- Woźniak, S.B., Stramski, D., 2004. Modeling the optical properties of mineral particles suspended in seawater and their influence on ocean reflectance and chlorophyll estimation from remote sensing algorithms. Appl. Opt. 43, 3489–3503. https://doi.org/10.1364/AO.43.003489.
- Woźniak, S.B., Stramski, D., Stramska, M., Reynolds, R.A., Wright, V.M., Miksic, E.Y., Cichocka, M., Cieplak, A.M., 2010. Optical variability of seawater in relation to particle concentration, composition, and size distribution in the nearshore marine environment at Imperial Beach, California. J. Geophys. Res. 115, C08027. https://doi.org/10.1029/2009ic005554.
- Woźniak, S.B., Sagan, S., Zabłocka, M., Stoń-Egiert, J., Borzycka, K., 2018. Light scattering and backscattering by particles suspended in the Baltic Sea in relation to the mass concentration of particles and the proportions of their organic and inorganic fractions. J. Mar. Syst. 182, 79–96. https://doi.org/10.1016/j. imarsys 2017 12 005
- Woźniak, S.B., Meler, J., 2020. Modelling water colour characteristics in an optically complex nearshore environment in the Baltic Sea: quantitative interpretation of the forel-ule scale and algorithms for the remote estimation of seawater composition. Remote Sens. 12, 2852. https://doi.org/10.3390/rs12172852.
- Xue, K., Ma, R., Wang, D., Shen, M., 2019. Optical classification of the remote sensing reflectance and its application in deriving the specific phytoplankton absorption in optically complex lakes. Remote Sens. 11, 184. https://doi.org/10.3390/ rs11020184
- Ye, H.J., Li, T., Shen, Q., Zhu, J., Wang, X., Zhang, F., Zhang, J., Zhang, B., 2016. Spectral classification of the Yellow Sea and implications for coastal ocean color remote sensing. Remote Sens. 8, 321. https://doi.org/10.3390/rs8040321.
- Zhang, X., Huot, Y., Bricaud, A., Sosik, H., 2015. Inversion of spectral absorption coefficients to infer phytoplankton size classes, chlorophyll concentration, and detrital matter. Appl. Opt. 54, 5805–5816. https://doi.org/10.1364/AO.54.005805.
- Zheng, G., Stramski, D., 2013. A model based on stacked-constraints approach for partitioning the light absorption coefficient of seawater into phytoplankton and nonphytoplankton components. J. Geophys. Res. Oceans 118, 2155–2174. https://doi. org/10.1002/jgrc.20115.
- Zheng, G., Stramski, D., Reynolds, R.A., 2014. Evaluation of the quasi-analytical algorithm for estimating the inherent optical properties of seawater from ocean color: comparison of Arctic and lower-latitude waters. Remote Sens. Environ. 155, 194–209. https://doi.org/10.1016/j.rse.2014.08.020.